

Galaxy gas flows inferred from a detailed, spatially resolved metal budget

F. Belfiore,^{1,2}★ R. Maiolino^{1,2} and M. Bothwell^{1,2}

¹Kavli Institute for Cosmology, University of Cambridge, Madingley Road, CB3 0HA Cambridge, UK

²Cavendish Laboratory, University of Cambridge, 19 J. J. Thomson Avenue, Cambridge CB3 0HE, UK

Accepted 2015 October 6. Received 2015 October 5; in original form 2015 March 24

ABSTRACT

We use the most extensive integral field spectroscopic map of a local galaxy, NGC 628, combined with gas and stellar mass surface density maps, to study the distribution of metals in this galaxy out to three effective radii (R_e). At each galactocentric distance, we compute the metal budget and thus constrain the mass of metals lost. We find that in the disc about 50 per cent of the metals have been lost throughout the lifetime of the galaxy. The fraction of metals lost is higher in the bulge (~ 70 per cent) and decreases towards the outer disc ($\sim 3 R_e$). In contrast to studies based on the gas kinematics, which are only sensitive to ongoing outflow events, our metal budget analysis enables us to infer the average outflow rate during the galaxy lifetime. By using simple physically motivated models of chemical evolution, we can fit the observed metal budget at most radii with an average outflow loading factor of order unity, thus clearly demonstrating the importance of outflows in the evolution of disc galaxies of this mass range ($\log(M_*/M_\odot) \sim 10$). The observed gas phase metallicity is higher than expected from the metal budget and suggests late-time accretion of enriched gas, likely raining on to the disc from the metal-enriched halo.

Key words: galaxies: abundances – galaxies: evolution – galaxies: fundamental parameters – galaxies: individual: NGC 628.

1 INTRODUCTION

Current models of galaxy evolution predict that star formation and consequent metal enrichment in galaxies are regulated by a combination of gas inflows and outflows. In this framework, the enrichment of the intergalactic medium (IGM) is mediated by metal-rich outflows produced by galactic winds, especially during the early, more active phases of galaxy evolution (Oppenheimer & Davé 2006; Scannapieco et al. 2006; Shen, Wadsley & Stinson 2010; Oppenheimer et al. 2012). Evidence for ongoing metal-enriched outflows has been obtained both through absorption line studies of quasars whose lines of sight cross the vicinity of nearby galaxies (Tumlinson et al. 2011, 2013; Bregman et al. 2013; Werk et al. 2013) and through direct imaging of outflowing ionized or neutral/molecular gas at low and high redshift (Heckman et al. 2000; Martin 2005, 2006; Veilleux, Cecil & Bland-Hawthorn 2005; Tremonti, Moustakas & Diamond-Stanic 2007; Feruglio et al. 2010; Sturm et al. 2011; Cano-Díaz et al. 2012; Maiolino et al. 2012; Arribas et al. 2014; Cazzoli et al. 2014; Ciccone et al. 2014, 2015). However, these observations are only probing ongoing events. A global understanding of the effect of outflows on the cosmic star formation history and IGM enrichment is only possible if we can gain insight into gas

flows over the entire evolutionary history of galaxies. The content and distribution of metals in galaxies can provide such information.

Metals are produced by stellar nucleosynthesis and act as a fossil record of a galaxy's star formation history and gas flows. Simple analytical models relating metal abundances to star formation rate (SFR) and gas flow rates have been presented by several authors (Erb 2008; Dayal, Ferrara & Dunlop 2013; Lilly et al. 2013; Ascasibar et al. 2014; Peng & Maiolino 2014) with the aim of explaining the scaling relations observed in statistical samples of galaxies. More detailed chemical evolutionary models have been successfully exploited to reproduce the observed chemical abundances, gas content and SFR of the solar neighbourhood, the Milky Way or nearby disc galaxies (Colavitti et al. 2009; Marcon-Uchida, Matteucci & Costa 2010; Spitoni & Matteucci 2011).

The common aim of chemical evolutionary models is to use chemical abundances observed today to infer the gas flow history and star formation history of the system. For example, in order to reproduce the chemical abundances of the Milky Way, a two-stage inflow model is generally invoked. The bulge is assumed to have formed at early times during a first inflow phase, while the disc is assumed to form inside-out during a second inflow phase (Matteucci & Francois 1989; Boissier & Prantzos 1999; Naab & Ostriker 2006; Williams et al. 2009). Hydrodynamical simulations of disc galaxies generally agree with the inside-out disc formation model (Pilkington et al. 2012). Chemical abundances can also provide clues on the relative importance of additional evolutionary processes in galaxies,

* E-mail: fb338@cam.ac.uk

including stellar migration, gas flows within the disc and large-scale galactic fountains.

Current large integral field spectroscopy (IFS) galaxy surveys (e.g. CALIFA, Sánchez et al. 2012; SAMI, Croom et al. 2012; MaNGA, Bundy et al. 2015) offer great potential for extending the study of resolved chemical abundances to much larger galaxy samples. Using optical IFS data, the chemical abundance of the interstellar medium (ISM) can be derived by analysing gas emission lines, while insight into the metallicity of the stellar population can be obtained using Lick indices, or applying spectral decomposition techniques (Cid Fernandes et al. 2011; Sánchez-Blázquez et al. 2014). The CALIFA survey has recently delivered important insights on the distribution of metals within star-forming galaxies, providing the strongest evidence so far for a universal gas-phase abundance gradient (Sánchez et al. 2014) out to two effective radii (R_e), as already suggested in previous work (Vila-Costas & Edmunds 1992; Bresolin et al. 2009; Bresolin, Kennicutt & Ryan-Weber 2012).

However, observations of resolved gas metallicity alone cannot be uniquely related to specific chemical evolutionary models and, unless measurements of the gas and stellar content are also available, the information provided by the gas metallicity is highly degenerate between inflows and outflows.

This work presents one of the first attempts to combine chemical abundances from IFS with gas mass measurements from millimetre/radio observations for a single galaxy (NGC 628) on the same spatial scales, along with stellar mass surface density and stellar metallicities. We are therefore able to constrain the metal budget both as a function of radius, and for the galaxy as a whole, out to $3 R_e$. Since we have access to information on radial gradients of the relevant physical quantities, we obtain an overall metal budget free from aperture effects, which affected previous work based on metallicities estimated from observations of galaxy central regions (for example from the SDSS galaxy sample, York et al. 2000; Abazajian et al. 2009).

Empirical studies of the metal budget in the $z = 0$ Universe, presented by several authors, agree in concluding that the total mass of metals produced by galaxies cannot be accounted for by the metals observed in stars and the ISM (Pettini et al. 1999; Ferrara, Scannapieco & Bergeron 2005; Bouché et al. 2007; Peebles & Shankar 2011; Zahid et al. 2012; Peebles et al. 2014). Large amounts of metals (between 35 per cent and 90 per cent) must be residing in the IGM, but also in the diffuse halo gas and in the circumgalactic medium (CGM). Although recent observational efforts have led to a better characterization of the metallicity of the gas in the hot halo phase (Tumlinson et al. 2011, 2013), a robust metal budget for these phases is still missing.

Cosmological hydrodynamical simulations which include chemical evolution in a self-consistent way generally agree with the empirical studies above, and highlight that the fraction of missing metals is strongly dependant of the sub-grid feedback prescription (Wiersma, Schaye & Theuns 2011; Pilkington et al. 2012).

The aim of this work is to investigate in detail how metals are lost from the galaxy, hence the severity of the ‘missing metal problem’. This information also provides tight constraints on the outflow loading factor (i.e. the ratio between SFR and outflow rate) averaged over the galaxy lifetime. The results are expected to provide simulators with new constraints on the net effect of gas flows in disc galaxies on resolved scales.

The paper is structured as follows. In Section 2, we give a brief overview of the observational data used; in Section 3, we summarize how we use the data to derive gas-phase metallicity, gas and stellar mass surface densities and their radial gradients. In Section 4, we

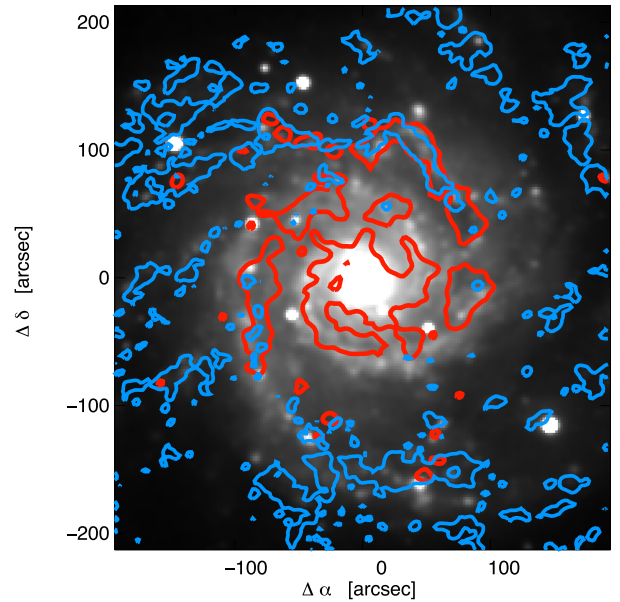


Figure 1. Optical image of NGC 628 (r' band from SDSS) with superimposed contours of H I (from the THINGS survey, in blue) and CO surface brightness (from the HERACLES survey, in red). The red contours correspond to a molecular hydrogen surface mass density of $10 M_{\odot} \text{pc}^{-2}$, while the blue H I contour correspond to a neutral hydrogen surface mass density of $12 M_{\odot} \text{pc}^{-2}$.

Table 1. General properties of NGC 628.

Property	Value
Name	NGC 628, M 74, UGC 1149
RA	00 ^h 59 ^m 50 ^s .1
Dec.	−07°34′41″.0
Type	SAC
Distance (adopted)	7.3 Mpc
i	7°
R_{24}	4′.88 = 10.3 kpc
R_e	67″ = 2.4 kpc
Scale	36 pc arcsec ^{−1}

summarize the chemical evolution framework, while in Section 5, we present the results on the metal budget and the modelling of the outflow loading factor in NGC 628. In Sections 6 and 7, we present the discussion and conclusions.

2 OVERVIEW OF THE DATA

NGC 628 is a nearby ($D \approx 7.3$ Mpc, $z = 0.00219$) nearly face-on ($i \approx 7^\circ$) spiral galaxy (Fig. 1). Table 1 summarizes some of its basic properties. NGC 628 is a good example of an isolated galaxy (no encounter in the last Gyr; see Kamphuis & Briggs 1992), displaying typical grand-design structure. The following sections describe the observations of NGC 628 that have been used in this work.

2.1 Integral field spectroscopy

In this study, we make use of IFS observations of NGC 628 taken as part of the PPAK IFS Nearby Galaxy Survey (PINGS; Rosales-Ortega et al. 2010, 2011; Sanchez et al. 2011). The survey was carried out using the 3.5 m telescope at the Calar Alto observatory, with the Potsdam Multi-Aperture Spectrograph in PPAK mode

Table 2. Multiwavelength observations of NGC 628 used in this work to supplement the IFS mosaic from Rosales-Ortega et al. (2010).

Telescope	Filter/Receiver	λ_{eff} (Å)	Bandwidth (Å)	PSF FWHM (arcsec)	Reference
GALEX	FUV	1516	268	4.3	Morrissey et al. (2007)
	NUV	2267	732	5.3	''
SDSS	u'	3540	599	1.49	Abazajian et al. (2009)
	g'	4770	1379	1.34	''
	r'	6222	1382	1.16	''
	i'	7632	1535	1.03	''
	z'	9060	1370	1.13	''
2MASS	J	1.235 (μm)	0.162 (μm)	2.5	Skrutskie et al. (2006)
	H	1.662 (μm)	0.251 (μm)	2.5	''
	K_s	2.159 (μm)	0.262 (μm)	2.5	''
Spitzer	IRAC1	3.550 (μm)	0.75 (μm)	1.66	Fazio et al. (2004)
	IRAC2	4.493 (μm)	1.01 (μm)	1.72	''
IRAM 30 m CO (2–1)	HERA	$\nu = 230.54$ (GHz)		13	Leroy et al. (2009)
VLA H I		$\nu = 1420.40$ (MHz)		5.57×6.80	Walter et al. (2008)

(Kelz et al. 2006). The PPAK fibre bundle corresponds to a field of view of $75 \text{ arcsec} \times 65 \text{ arcsec}$ and consists of 331 science fibres of $2''.7$ diameter packed in a hexagonal pattern, leading to a filling fraction of 65 per cent.

The data cover the spectral range between 3700 \AA and 7100 \AA , with a spectral resolution of full width at half-maximum (FWHM) $\sim 8 \text{ \AA}$. Due to the large projected size of the galaxy ($10''.5 \times 9''.5$) the data consist of a mosaic of observations taken on six different nights over a period of three years. The final size of the mosaic is of $6 \text{ arcmin} \times 7 \text{ arcmin}$. We estimate the PSF to have an FWHM of approximately 3 arcsec .

2.2 H I 21 CM OBSERVATIONS

We used observations of the 21 cm line from THINGS (The H I Nearby Galaxy Survey, Walter et al. 2008). This survey comprises 34 nearby galaxies observed with the Very Large Array (VLA), at high spectral ($< 5.3 \text{ km s}^{-1}$) and spatial resolution. NGC 628 was observed using the B, C and D configurations with a combined on-source integration time of $\sim 10 \text{ h}$. We use the publicly available¹ ‘robust’ weighted map (the ‘robust’ weighting scheme is used to achieve a sensitivity close to natural weighting while preserving a resolution close to uniform weighting, see Walter et al. 2008 for details), which has a beam size of $\approx 6 \text{ arcsec}$ ($B_{\text{min}} = 5''.57$, $B_{\text{maj}} = 6''.8$). The 1σ noise per 2.6 km s^{-1} channel is $0.66 \text{ mJy beam}^{-1}$, corresponding to a sensitivity of $\approx 0.5 M_{\odot} \text{ pc}^{-2}$, sufficient to trace the atomic hydrogen in all regions where it constitutes the dominant component of the ISM.

2.3 CO(2–1) observations

Observations of the CO(2–1) transition were used to infer the molecular gas content. Maps are obtained from the publicly available² HERA CO-Extragalactic Survey (HERACLES; Leroy et al. 2009). HERACLES is a survey of 48 nearby galaxies using the HERA multipixel receiver on the IRAM 30 m telescope, with 13 arcsec angular resolution and 2.6 km s^{-1} spectral resolution. The 1σ sensitivity of the map is estimated to be $\approx 3 M_{\odot} \text{ pc}^{-2}$ (with the Galactic conversion factor discussed in Section 3).

¹ <http://www.mpia.de/THINGS/Data.html>

² <http://www.mpia-hd.mpg.de/HERACLES/Data.html>

2.4 Multiwavelength photometric data

Photometry in different bands was collected to obtain a reliable estimate of the stellar mass surface density by performing pixel-by-pixel spectral energy distribution (SED) fitting. We collected observations from Galaxy Evolution Explorer (GALEX), Two Micron All Sky Survey (2MASS) and the Spitzer Space Telescope IRAC camera. In the optical band, we make use of the photometry from SDSS Data Release 7. Table 2 summarizes the basic properties of the data set used and the relevant references.

3 DATA ANALYSIS

In this section, we present the analysis performed on the reduced data to obtain gas-phase metallicities, stellar mass surface density and gas mass surface density profiles. We also briefly discuss the adopted choice of gas-phase metallicity calibrators (Section 3.2) and the radial gradients of the derived quantities (Section 3.6). Throughout the section we highlight potential sources of systematic uncertainty.

3.1 Emission line fluxes

We extract emission line fluxes in each spaxel from the IFS datacube following a very similar procedure to Belfiore et al. (2015). Here we give a brief overview of the main steps involved.

(i) For each spaxel, we fit a linear combination of single stellar population (SSP) templates, after correction for systemic velocity and instrumental dispersion, using Penalized Pixel Fitting (Cappellari & Emsellem 2004). In this work, we used a grid of 29 SSP templates, generated by using Maraston & Stromback (2011) models based on the empirical STELIB spectral library (Le Borgne et al. 2003). A spectral region of 600 km s^{-1} is masked around each emission line we wish to fit. Strong sky lines are also masked. We do not attempt to extract stellar population parameters from the SSP fits. Such a study has recently been carried out by Sánchez-Blázquez et al. (2014), and in Section 5.1 we make use of the stellar metallicity gradient derived in their work.

(ii) For each spaxel, we subtract the stellar population fit from the observed spectrum to obtain a pure emission line spectrum. This is then fitted with a set of Gaussian functions, one per emission line (using least-squares minimization). The doublets

[O III] $\lambda\lambda$ 4959, 5007 and [N II] $\lambda\lambda$ 6548, 6584 are set to have the same velocity and velocity dispersion and the ratio of their intensities is fixed to the theoretical one. We calculate emission line fluxes by integrating the flux under the fitted Gaussians.

(iii) We apply a signal to noise cut to the emission line maps generated above, imposing a S/N larger than 5 in H α and H β . This threshold is intentionally high to exclude regions of diffuse emission (mainly inter-arm regions), where the H α emission might not be ascribed to bona fide H II regions. We also discard regions where both the [O II] and the [O III] line are undetected.

(iv) We calculate the reddening from the Balmer decrement, by using the H α /H β ratio and a Calzetti (2001) attenuation curve with $R_V = 4.05$. The theoretical value for the Balmer line ratio is taken from Osterbrock & Ferland (2006), assuming case B recombination (H α /H $\beta = 2.87$). We note that the use of extinction curve of Cardelli, Clayton & Mathis (1989) (or the modification by O'Donnell 1994) with $R_V = 3.1$ yields very similar results for the 3600 Å to 7000 Å wavelength range considered in this work.

3.2 Gas-phase metallicity

Reliably measuring the gas metallicity from emission lines ratios remains a difficult problem in observational astrophysics. Different line ratios ('diagnostics') and methods ('calibrations') have been developed for the task. However, it is well known that different calibrations, even when based on the same diagnostics, can give results differing by up to 0.6 dex (Kewley & Ellison 2008; López-Sánchez et al. 2012; Peña Guerrero, Peimbert & Peimbert 2012). It is beyond the scope of this work to resolve the abundance scale problem (but see recent advances towards a possible solution in Dopita et al. 2013; Pérez-Montero 2014; Blanc et al. 2015). Fixing the gas-phase metallicity scale is, however, a key factor in determining the total metal budget. We therefore discuss some of the assumptions going into widely used metallicity calibrators and possible shortcomings of each.

The metallicity (i.e. the oxygen abundance $12 + \log(\text{O}/\text{H})$, where O and H are number densities), can be calculated knowing the electron temperature, which can be derived from the ratio of the oxygen auroral line [O III] λ 4363 and another oxygen line, like [O III] λ 5007. This method (referred to as the T_e method³) is generally considered one of the most reliable, at least in the low-metallicity regime (Garnett 1992; Pagel et al. 1992; Izotov et al. 2006). At high metallicities, however, the electron temperature decreases and the auroral line is generally undetected. Moreover, temperature fluctuations make the T_e method unreliable at high metallicities (Stasinska 2005; Bresolin 2007). Due to the strong temperature dependence of the emissivity of the auroral lines, regions with higher than average temperature may dominate the line emission, hence biasing the metallicity measurements towards low values. Finally, there is evidence that the distribution of electron energies in H II regions might not follow a Boltzmann distribution (Binette et al. 2012; Nicholls et al. 2013), hence making the definition of temperature arguable, while a κ -distribution may be more appropriate (Dopita et al. 2013).

Recombination lines can also be used to estimate the metallicity. These are almost insensitive to temperature, which makes them much less dependent on temperature fluctuations and on the specific

distribution of electron energies. However, these lines are approximately 10^4 times fainter than H β , which makes their detection possible only for bright sources on 8 m class telescopes. Metallicities estimated from the recombination lines are systematically offset, by about 0.2 dex, compared to those measured with the T_e method (Blanc et al. 2015). Some authors (Peimbert & Peimbert 2010; Peña Guerrero et al. 2012) attribute this discrepancy to the presence of small temperature fluctuations within H II regions, which (as discussed above) would bias the observed auroral line fluxes towards the highest temperature, lower abundance regions.

Finally, several authors have calibrated strong nebular line ratios (making use of [O III] $\lambda\lambda$ 4959, 5007, [O II] λ 3727, [N II] λ 6584, etc.) as abundance diagnostics. While the intensity of these lines depends on several factors besides the metal abundance (ionization parameter, density, N/O ratio), calibrations take advantage of the fact that in the H II regions observed in the local Universe relations exist between some of these parameters. Strong line diagnostics can be calibrated against T_e -based metallicity measurements (Pettini & Pagel 2004; Pilyugin & Thuan 2005; Pilyugin, Vílchez & Thuan 2010), photoionization models (Denicolo, Terlevich & Terlevich 2002; Kobulnicky & Kewley 2004; Tremonti et al. 2004), or a mixture of both (Nagao, Maiolino & Marconi 2006; Maiolino et al. 2008). Recently, Blanc et al. (2015) has shown that some (but not all) photoionization model grids are able to reproduce the metallicities measured using recombination lines.

To take into account the systematic uncertainty introduced by the choice of metallicity calibration, in this work we use two independently derived calibrations.

(i) The calibration from Maiolino et al. (2008) (M08), which is based on photoionization models (Kewley & Dopita 2002) in the high-metallicity regime and anchored to T_e -based metallicity measurements in the low-metallicity regime. While M08 provides calibrations for various strong line diagnostics, here we use only the calibration based on the R23 parameter,

$$R23 = ([\text{O II}]\lambda 3727 + [\text{O III}]\lambda 4959 + [\text{O III}]\lambda 5007)/\text{H}\beta.$$

In the context of this work, we have re-calculated the parametrization of the R23-metallicity relation using the same procedure in M08, but using a fifth-order polynomial fit (M08 used a fourth-order polynomial) to provide a better fit to the high-metallicity end of the relation between $12 + \log(\text{O}/\text{H})$ and R23. Overall the M08 calibration gives similar abundances to those obtained using the calibration used by Tremonti et al. (2004) and the calibration of R23 presented by Kobulnicky & Kewley (2004). Since the R23 parameter is double valued, we break the degeneracy by using the [N II]/[O II] ratio, concluding that all the regions in NGC 628 belong to the upper branch of R23. We have tested the use of a calibration that recursively solves for metallicity and ionization parameter (Kobulnicky 2004) and found that the derived metallicities are not substantially altered.

(ii) The calibration from Pettini & Pagel (2004) (PP04), based mostly on T_e measurements, using the O3N2 index:

$$\text{O3N2} = \log \frac{[\text{O III}]\lambda 5007/\text{H}\beta}{[\text{N II}]\lambda 6584/\text{H}\alpha}$$

This calibration has the disadvantage of depending explicitly on the nitrogen abundance, which does not necessarily scale in a simple way with the oxygen abundance (Pérez-Montero & Contini 2009; Pérez-Montero 2014; Belfiore et al. 2015), since nitrogen has both a primary and a secondary nucleosynthetic origin and is released into the ISM on longer timescales than oxygen.

³ Or sometimes as the 'direct method'. However, given the well-known systematic uncertainties in T_e -measured metallicities, we feel that this designation is inappropriate

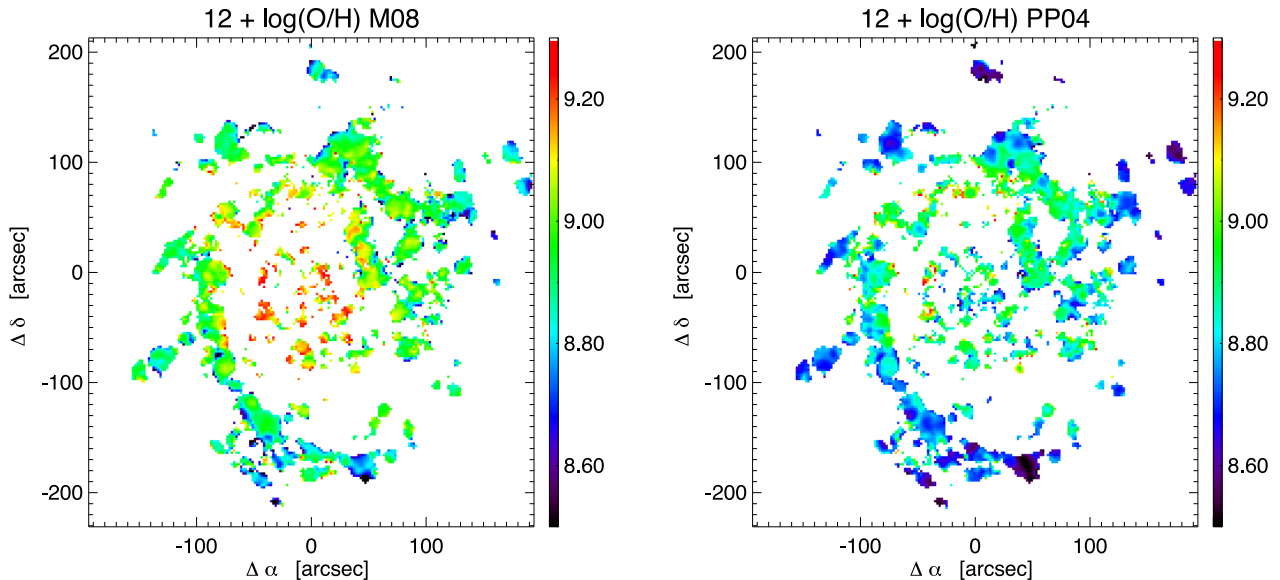


Figure 2. Maps of the gas metallicity in NGC 628 using the Maiolino et al. (2008) (M08) calibration based on R23 (left) and the Pettini & Pagel (2004) (PP04) calibration based on O3N2 (right). Only spaxels that lie below the Kewley et al. (2001) demarcation line in the $[\text{O III}]/\text{H}\beta$ versus $[\text{S II}]/\text{H}\alpha$ BPT diagram are included.

It is also worth noting that we are (perhaps unduly) extending the PP04 calibration to super-solar metallicities. In the original work of Pettini & Pagel (2004), only two H II regions with super-solar metallicity and T_e measurements are presented, while the high-metallicity end of the calibration is fixed by considering a small number of regions with metallicities calculated using photoionization models. Even in the most recent calibration of the O3N2 diagnostic, presented by Marino et al. (2013), only five H II regions with super-solar metallicity are included, which makes any attempt to ‘directly’ calibrate the relation between O3N2 and metallicity in the super-solar regime subject to large extrapolation uncertainties.

We also note that the two adopted calibrations make different assumptions regarding dust depletion of oxygen. In the M08 calibration, an oxygen depletion factor of 0.22 dex is assumed (Kewley & Dopita 2002), while T_e -based calibrations do not correct for the amount of oxygen depleted on to dust. We follow Peimbert & Peimbert (2010) and Peña Guerrero et al. (2012) and modify the metallicities obtained from both calibrations assuming a constant oxygen depletion factor of 0.1 dex. For the rest of this work we will use gas-phase metallicity to refer to the overall oxygen abundance of the ISM (gas and dust), with the understanding that the dust is taken into account through a constant depletion factor. Altering the dust depletion by ± 0.1 dex does not substantially change any of our conclusions.

Since M08 and PP04 are representative of the two main classes of metallicity calibrators (T_e -based and photoionization-model-based), alternative calibrations will not lead to metallicity estimates significantly higher than M08 or significantly lower than PP04. A thorough analysis of the gas-phase metallicity in NGC 628 was presented in Rosales-Ortega et al. (2011), who used a similar set of calibrators (as noted above, the Kobulnicky & Kewley 2004 calibration is roughly equivalent to the adopted Maiolino et al. 2008) and obtained similar gradients and zero-points to the ones presented in this work. Interestingly, recent work from Croxall et al. (2013), who used far-IR lines to estimate metallicity in NGC 628, points towards oxygen abundances within the range bracketed by the M08 and PP04 calibrations. Additionally Berg et al. (2015) obtained

direct T_e measurements of metallicity for 45 H II regions in NGC 628, which agree on average, though with large scatter, with the metallicities derived with the PP04 calibration. The reason for the large scatter in the T_e -derived metallicities is not clear, but according to Berg et al. (2015) might be due to systematics in their electron temperature measurements.

Since metallicity diagnostics are only calibrated for star-forming regions (classical H II regions), regions of galaxies where other types of ionization (shocks, active galactic nuclei, evolved stars, etc.) are dominant should be excluded. We use the standard ionization diagnostic diagram (BPT diagram Baldwin, Phillips & Terlevich 1981; Veilleux & Osterbrock 1987; Kewley et al. 2001; Kauffmann et al. 2003) to identify galactic regions as star-forming and discard regions that lie above the Kewley et al. (2001) demarcation line in the $[\text{O III}]/\text{H}\beta$ versus $[\text{S II}]/\text{H}\alpha$ diagnostic diagram. All of the discarded spaxels are found in the inter-arm regions and present LINER-like (low ionization nuclear emission-line regions) ionization, which might be due to evolved hot stars dominating the ionization budget in regions where no recent star formation has taken place (Yan & Blanton 2012; Belfiore et al. 2015). We note that such regions, not complying with the H II classification, are only 5 per cent of the total, and their exclusion does not affect our final results.

The resulting maps of gas-phase metallicity for the M08 and PP04 calibrations are shown in Fig. 2. For reference, the photospheric solar oxygen abundance, as derived by Asplund et al. (2009), is $12 + \log(\text{O}/\text{H}) = 8.69$, or equivalently $Z_{\odot}(\text{O}) = 0.00585$. Note that we are referring to Z as the oxygen abundance by mass. The total metal content (fraction by mass of elements heavier than helium) in the Sun is 0.0142.

3.3 Stellar mass surface density

Stellar mass surface densities are estimated by performing SED fitting in each pixel on the multiwavelength photometric data from UV to near-IR, using the software package CIGALE (Code Investigating GALaxy Emission, Burgarella, Buat & Iglesias-Páramo 2005; Noll

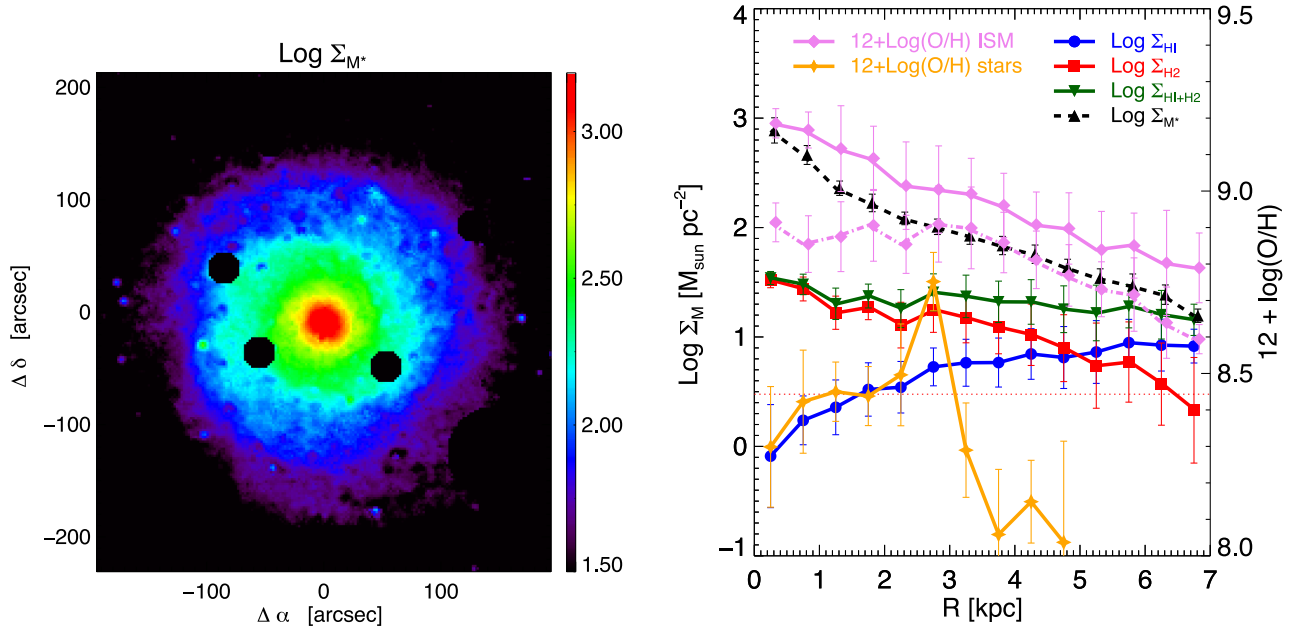


Figure 3. Left: stellar mass surface density map, created from the spatially resolved SED fitting. Foreground stars have been masked. Right: radial dependence of various physical quantities across the disc of NGC 628 (in radial bins; error bars represent the scatter in each radial bin). Atomic gas surface density (blue) shows a dip in the central region, while the molecular gas surface density (red) is peaked at the centre and quickly decreases outwards. The horizontal red dashed line corresponds to the sensitivity limit of the CO observations. The total gas content (green) is nearly flat across the whole disc up to $3 R_e$ ($1 R_e = 2.4$ kpc). A clear radial gradient is observed in both stellar mass surface density (black, short dashes) and gas metallicity (violet). The latter is shown both for the M08 (solid violet) and PP04 (dot-dashed violet) metallicity calibrations. The stellar metallicity gradient from Sánchez-Blázquez et al. (2014) is shown in orange. Note that the metallicities of gas and stars are plotted with respect to the alternative y-axis on the right in units of $12 + \log(\text{O}/\text{H})$.

et al. 2009). In detail, we followed the procedure outlined below (similar to Boquien et al. 2012).

(i) The different observations were smoothed to the lowest resolution of the photometric data set (*GALEX* NUV), using the kernels from Aniano et al. (2011).

(ii) The maps were then regridded on the same pixel scale as the IFS mosaic.

(iii) For each pixel, the flux and the flux error in each band was extracted. Errors are computed by taking into account the uncertainty in absolute calibration of the different instruments. Fluxes and errors are used as input for the software package *CIGALE*.

(iv) *CIGALE* creates FUV-to-FIR SEDs consisting of dust-attenuated complex stellar population models. In this analysis, we used Maraston (2005) templates (with a Kroupa IMF) to build a grid of stellar models with a range in metallicity (from 0.5 to 2 solar). The star formation history is parametrized by an exponentially decreasing SFR, and an old stellar population with and a grid of younger stellar population bursts. Extinction is fitted using a Calzetti-like attenuation curve. The optimal galaxy parameters are derived by *CIGALE* using a Bayesian-like analysis. A map of stellar mass surface density is then created (Fig. 3, left-hand panel)

The formal errors computed by *CIGALE* (which take into account the uncertainty in the data, but not the systematics of the method) are of the order of 0.1 dex. As a further check, we compared the stellar mass estimated by *CIGALE* with the stellar mass estimate obtained using the procedure in Bell et al. (2003) and using the $u-r$ colour to estimate the mass-to-light ratio. The stellar mass densities obtained with the Bell formulation are consistent with the ones obtained with *CIGALE*, with a small systematic difference of less than 0.1 dex at

very large radii ($R > 8$ kpc). The total mass of NGC 628 out to $3 R_e$ computed by *CIGALE* is $\log(M_*/M_\odot) = 9.8$.

3.4 Stellar metallicity

To take into account the metals locked in stars, we make use of the recent study of Sánchez-Blázquez et al. (2014), who present the mass-weighted stellar metallicity gradient for NGC 628 by performing full spectral fitting using the software package *STECKMAP* on the PINGS IFS data. Despite the increased level of sophistication of the spectral fitting algorithms in recent years (Heavens, Jimenez & Lahav 2000; Panter, Heavens & Jimenez 2004; Fernandes, Sodr & Gomes 2005; Gallazzi et al. 2006; Sánchez-Blázquez et al. 2011; Cid Fernandes et al. 2014; McDermid et al. 2015; Wilkinson et al. 2015), stellar metallicity remains the hardest quantity to estimate in stellar population studies. The difficulty is due to the non-linear effect of a limited set of metallicity values generally available in spectral libraries (since most stellar libraries rely on observations in the solar neighbourhood super-solar metallicity stars are not well represented) and the well-known age–metallicity degeneracy (e.g. Worthey et al. 1994), which acts in the direction of confusing old, metal-poor systems with young metal-rich ones. While the ability of spectral fitting codes to reliably derive input parameters increases as a function of S/N, it has been shown (see for example, Cid Fernandes et al. 2014; Wilkinson et al. 2015) that even for high S/N spectra, stellar metallicity calculated with different sets of simple stellar populations can differ by more than 0.2 dex. It is beyond the scope of this work to perform a new full spectral fitting study of the PINGS data for NGC 628 and further evaluate these systematic uncertainties. We note, however, that our simple approach of propagating of the errors in the stellar metallicities presented in

Sánchez-Blázquez et al. (2014) (median error ~ 0.15 dex) might represent an underestimate of the real uncertainty.

Taking into account the necessary correction factor due to the fact that Sánchez-Blázquez et al. (2014) adopt a different distance for NGC 628, we can obtain a stellar metallicity gradient out to 5 kpc. We put the gas-phase and stellar metallicity on the same abundance scale by using the solar metallicity of Asplund et al. (2009) and assuming solar abundance ratios. We do not attempt to correct for possible non-solar abundance ratios (e.g. α -enhancement) in the bulge, since in any case the correction will only affect our innermost radial bin and will not have a significant effect on the subsequent analysis of integrated properties.

3.5 Gas mass surface density

The H I mass can be calculated directly from the H I surface brightness, assuming that H I is everywhere optically thin.

To convert from CO luminosity to H₂ mass we adopt a constant CO to H₂ (α_{CO}) conversion factor given by

$$\alpha_{\text{CO}} = 4.35 \frac{M_{\odot} \text{ pc}^{-2}}{\text{K km s}^{-1}}.$$

This value of the conversion factor is appropriate for the Milky Way (Solomon et al. 1987; Strong & Mattox 1996; Abdo et al. 2010; Bolatto, Wolfire & Leroy 2013). We explored the effect of using a metallicity-dependant conversion factor (Schrubba et al. 2011) and the conversion factor derived by Blanc et al. (2013) by inverting the star formation law in NGC 628, finding that none of our conclusions are substantially modified. As the conversion factors are calibrated for the CO (1–0) line, while the HERACLES observations map the CO (2–1) transition, we assume a constant ratio of 0.7 between the two CO luminosities (Leroy et al. 2012).

To calculate the total gas mass we multiply the H I component by 1.36 to account for helium and add the molecular gas mass computed using the conversion factor above, which already takes helium into account.

3.6 Radial gradients

It is well known that spiral galaxies exhibit radial gradients in their physical properties, including stellar mass surface density and metallicity (Bell & de Jong 2001; Moustakas et al. 2010; González Delgado et al. 2013; Sánchez et al. 2014).

In Fig. 3, we present the radial gradients for the different physical quantities that we have derived in this section for NGC 628. We observe an exponential profile in stellar mass surface density and gas-phase metallicity (black dashed and violet lines, respectively).

We note here that the PP04 gas metallicity gradient presents a flattening in the inner 2.5 kpc ($\approx 1R_{\text{e}}$, violet dot-dashed line), already reported in previous work (Rosales-Ortega et al. 2011) and consistent with the flattening observed in a subsample of galaxies from the CALIFA survey (Sánchez et al. 2014). With the current data it is not possible to assess whether this feature corresponds to a real abundance drop in the central region or if it is an artefact of the metallicity calibration. In particular, we note that such flattening observed when using the O3N2 calibration is often associated with a central decrease of the N/O abundance ratio (which can be traced by the [N II]/[O II] flux ratio), and this is also the case of NGC 628. Therefore, the metallicity flattening may actually reflect a relative abundance variation affecting the metallicity diagnostic used in PP04, rather than a global metallicity flattening. However, we note that from the theoretical standpoint, bars and

other non-axisymmetric perturbations can trigger large-scale gas flows and induce a flattening of the metallicity gradient (Roskar et al. 2008b,a; Cavichia et al. 2013), together with a metallicity ‘hump’ at the interface. While the gas-phase abundance does not show evidence for this hump, a sharp increase in the stellar metallicity is reported at 2.5 kpc by Sánchez-Blázquez et al. (2014; orange line in Fig. 3). They interpret this feature as the effect of an oval distortion (possibly a signature of a dissolving bar). The presence of a circum-nuclear ring of enhanced star formation seems to confirm this hypothesis.

The H I disc is much more extended than the FoV of the IFS data and presents clumpy substructure (seen in Fig. 1). The H I surface density profile is characterized by a central dip and an increase towards larger radii. The maximum in H I surface density coincides roughly with the edge of the IFS field of view ($\approx 3R_{\text{e}}$), hence in our subsequent analysis, which is limited to the radial extent of the IFS observations, we neglect about 40 per cent of the mass of the H I disc. We will discuss the importance of this extended H I disc in Section 6.

The molecular gas profile is centrally concentrated and its surface density decreases with radius. The sensitivity limit of the HERACLES data is shown as a horizontal dotted line in Fig. 3. The combination of the atomic and molecular gas profile generates a total gas surface density profile (green line in Fig. 3) which is remarkably constant over the whole field of view of the IFS data. This implies that the gas fraction ($f_{\text{gas}} = M_{\text{gas}}/(M_{\star} + M_{\text{gas}})$) increases outwards roughly log-linearly with radius.

4 THE CHEMICAL EVOLUTION FRAMEWORK

In this section, we present the analytical framework we will be using to study the metallicity evolution in resolved regions of NGC 628.

We make use of simple relations obtained by invoking the instantaneous recycling approximation and perfect instantaneous mixing. This framework has been proven successful in modelling the chemical evolution of oxygen (Zahid et al. 2012; Dayal et al. 2013; Peebles et al. 2014; Peng & Maiolino 2014), which is predominantly produced by short-lived massive stars dying as core-collapse supernovae. We note in passing that the chemical abundances of other common elements (like N or Fe) require a more detailed model, taking into account stellar lifetimes, the Type Ia supernovae delay time distribution and variation of the nucleosynthetic yields with metallicity, and will not be attempted in this work. However, since oxygen is the most abundant metal by mass, it is a good tracer for the total metal content.

Several studies in the literature have shown that, in order to interpret observed chemical abundances in galaxies, it is necessary to devise a model taking gas inflows and outflows into account (often dubbed the ‘gas regulatory’ or ‘bathtub’ models; Matteucci 1986; Gibson et al. 2003; Lilly et al. 2013; Dekel & Mandelker 2014; Peng & Maiolino 2014).

Within the instantaneous recycling approximation, denoting the oxygen fraction (by mass) in the ISM as Z_{g} , the gas mass as M_{g} , the star formation rate as SFR, the stellar mass as M_{\star} , the total mass in oxygen in the galaxy as M_{Z} , the mass of oxygen in the ISM as M_{Zg} , the outflow rate as Ψ and the inflow rate as Φ , the galaxy’s chemical evolution in a bathtub model is described by the following constitutive equations

$$\frac{dM_{\text{g}}}{dt} = \Phi - (1 - R) \text{SFR} - \Psi, \quad (1)$$

$$\frac{dM_\star}{dt} = (1 - R) \text{SFR}, \quad (2)$$

$$\frac{dM_{Z_g}}{dt} = \frac{d(M_g Z_g)}{dt} = p \text{SFR} - \Psi Z_g - (1 - R) Z_g \text{SFR}, \quad (3)$$

and

$$\frac{dM_Z}{dt} = p \text{SFR} - \Psi Z_g, \quad (4)$$

where p is the mass of newly synthesized oxygen per unit mass of gas converted into stars (we will refer to it as the *yield* per stellar generation) and R is the fraction of gas mass that is promptly returned to the ISM via stellar mass-loss processes (referred to as the *return fraction*). We emphasize that the same relations apply also to the total abundance of metals (after replacing the appropriate value for the net nucleosynthetic yield), if the abundance ratios of different elements are assumed constant.

Both the average yield and the return fraction are a function of the initial mass function (IMF) and in general also depend on metallicity and time. In our simple model, neither the time nor the metallicity dependence of R and y will be further considered, since the oxygen yield is shown to be approximately independent of metallicity and the effect of stellar lifetimes on the return fraction can be considered negligible for our purposes (Thomas, Greggio & Bender 1998; Kobayashi et al. 2006; Zahid et al. 2012; Vincenzo et al. 2015).

If we denote as $p(M)$ the net yield of oxygen for stars of mass M , then the net yield (p) per stellar generation is given by

$$p = \frac{\int_{M_{\text{long-liv}}}^{M_{\text{up}}} p(M) \text{IMF}(M) dM}{\int_{M_{\text{low}}}^{M_{\text{up}}} \text{IMF}(M) dM}, \quad (5)$$

where the $\text{IMF}(M)$ is the initial mass function, M_{low} and M_{up} are the lower and upper mass cutoffs of the IMF, while $M_{\text{long-liv}}$ is the highest mass of the stars that are considered ‘eternal’ or, equivalently, the lowest mass of the stars contributing to the chemical enrichment. Note that an alternative definition of yield is given by the new mass of oxygen produced per unit mass of long-lived stars (Searle & Sargent 1972) (in this case generally denoted as y). These two definitions are trivially related by the return fraction with $y = p/(1 - R)$.⁴ It is important to stress that the yield per stellar generation is strongly dependent on the IMF, and not only on the ‘stellar’ nucleosynthetic yield $p(M)$. In fact, the average yield can vary by a factor larger than 3 for the same choice of stellar yields if the IMF is changed from Kroupa, Tout & Gilmore (1993) to Chabrier (2003) (Vincenzo et al. 2015).

In this work, when a numerical value for the average yield is required, we make use of the results in Vincenzo et al. (2015), based on the compilation of stellar yields in Romano et al. (2010), which have been shown to successfully reproduce the oxygen abundance in the Milky Way. We adopt a Kroupa et al. 1993 IMF, $M_{\text{long-liv}} = 1 M_\odot$ and therefore get a fiducial average yield of $p = p_O = 0.007$ for oxygen and $R = 0.30$ (Vincenzo et al. 2015). The same results can be applied to the *total* content of metals, by replacing the numerical value of the average yield with $p = p_Z(\text{tot}) = 0.013$.

⁴ Note that Peng & Maiolino (2014) does not follow this traditional notation. The quantity denoted as y in Peng & Maiolino (2014) is the same quantity which we denote as p in this work.

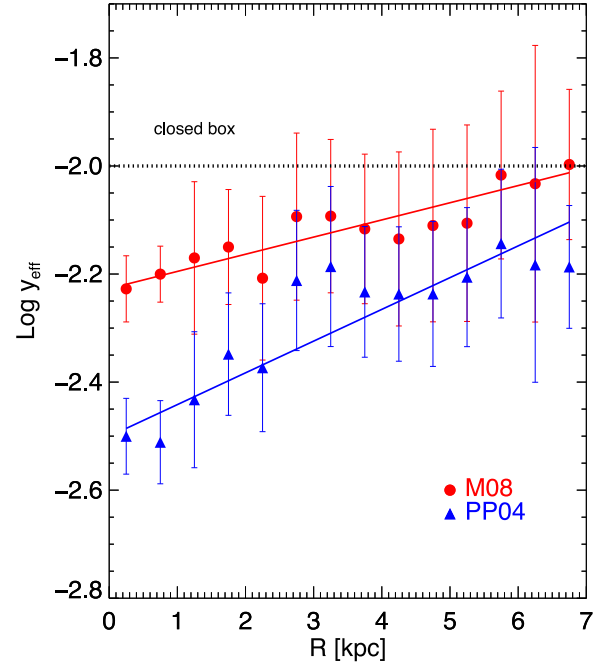


Figure 4. The radial variation of the effective yield in NGC 628. The value expected for the closed box case, $y = p/(1 - R) = 0.010$, is indicated as a black dotted line. The red circles and blue triangles represent, respectively, the results obtained with the Maiolino et al. (2008) and Pettini & Pagel (2004) calibrations.

It can be easily shown that in the case of a ‘closed box’ evolution, i.e. no inflow and no outflow ($\Phi = 0$ and $\Psi = 0$), the gas metallicity is given by

$$Z_g = \frac{p}{1 - R} \ln(f_{\text{gas}}^{-1}) = y \ln(f_{\text{gas}}^{-1}), \quad (6)$$

where $f_{\text{gas}} \equiv M_g/(M_g + M_\star)$ is the gas fraction. Some authors find convenient to define the so-called effective yield as

$$y_{\text{eff}} \equiv \frac{Z_g}{\ln(f_{\text{gas}}^{-1})}. \quad (7)$$

Whenever $y_{\text{eff}} \neq y = p/(1 - R)$, equation (6) implies that the system has not evolved as a closed box. Fig. 4 shows the radial gradient of the effective yield in NGC 628, clearly demonstrating that y_{eff} increases with radius. Importantly, the observed effective yield is always lower than $y = p/(1 - R) = 0.010$, implying that the region of the disc of NGC 628 sampled by us has not been evolving as a closed box.

However, the information provided by the effective yield is highly degenerate. More specifically, both enriched gas outflows or pristine (or low metallicity) gas inflows will lead to the observed effective yield to be lower than the closed box value (Edmunds 1990).

5 RESULTS

5.1 A spatially resolved oxygen mass budget

The aim of this section is to compute the total mass of oxygen present in NGC 628 as a function of radius and compare it with the total mass of oxygen expected to have been produced by its stellar component.

This comparison provides a direct (model-independent) measurement of the mass of metals lost by each region in the galaxy via

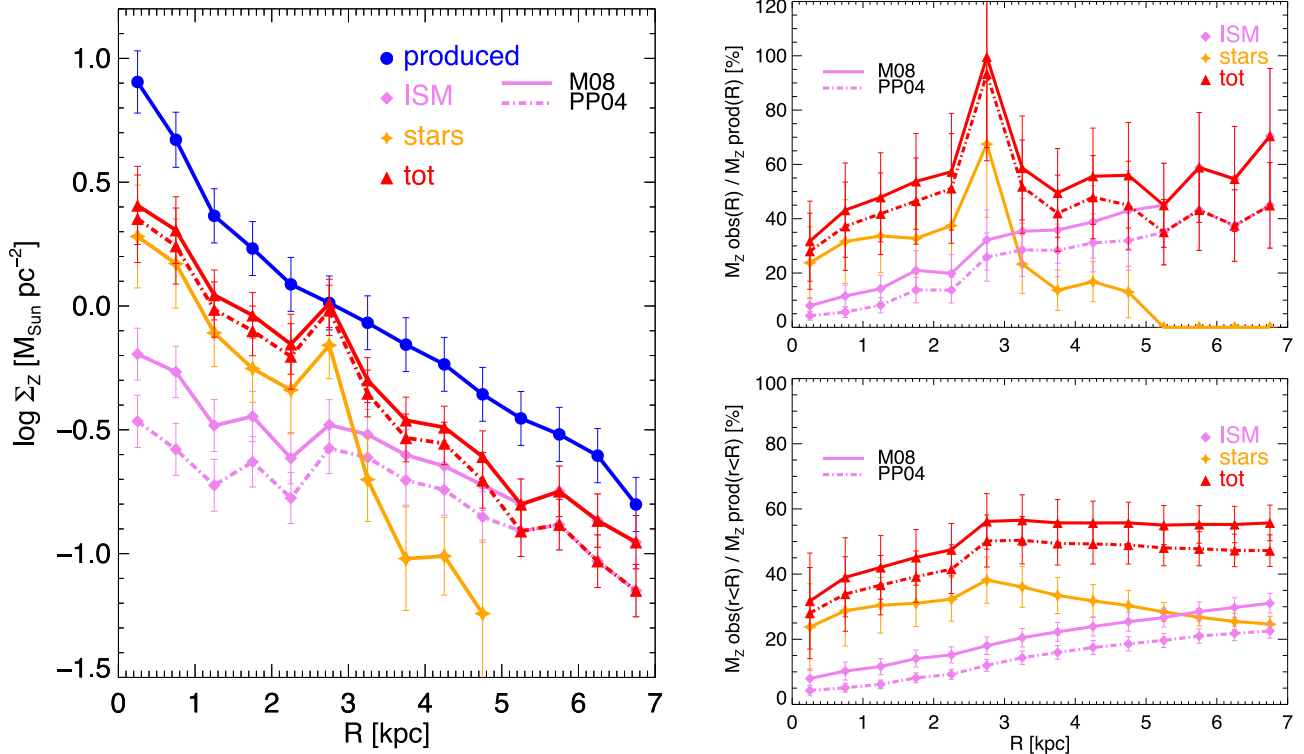


Figure 5. Left: oxygen mass per unit area in different galactic components compared with the oxygen mass expected to have been produced by the observed stars, in different radial bins. The orange line shows the oxygen mass locked in stars, by using the stellar metallicity gradient from Sánchez-Blázquez et al. (2014). The violet solid line shows the oxygen mass in the ISM obtained by using the M08 calibration, while the violet-dashed line shows the oxygen mass in the ISM obtained by using the PP04 calibration. In red, we show the total observed mass of oxygen (ISM + stars). The blue line shows the mass of oxygen produced by the stars at the same location assuming our fiducial average yield. Top right: mass of oxygen in each radial bin as a percentage of the mass of oxygen produced in the same radial bin. The colour-coding is the same as in the left-hand panel. Bottom right: the cumulative mass of oxygen within radius R in the different galactic component, expressed as a percentage of the total mass of oxygen produced within the same radius R . The points shown for the last radial bin correspond to the integrated oxygen budget for NGC 628, showing that the galaxy as a whole has retained only ≈ 50 per cent of the metals it has produced.

metal-enriched outflows. Moreover, the results obtained in this section can be directly compared with predictions from cosmological simulations.

Following equation (4), the total mass of oxygen *produced* is given by

$$M_{Z\text{-prod}} = y M_{\star}. \quad (8)$$

This corresponds to the total mass of oxygen actually present in the galaxy in the case of no outflows (equation (4) with $\Psi = 0$). The total observed mass of oxygen is given by the sum of the mass of oxygen in the ISM ($M_{Zg} = Z_g M_g$) and the mass of oxygen locked in stars ($M_{Z\star} = Z_{\star} M_{\star}$), i.e.

$$M_{Z(\text{obs,tot})} = M_{Zg} + M_{Z\star} = Z_g M_g + Z_{\star} M_{\star}. \quad (9)$$

Both simulations (Marinacci et al. 2014) and observations (Shull, Smith & Danforth 2012; Tumlinson et al. 2013) argue that a large quantity of baryons and metals might reside in the hot haloes around galaxies. However, for the purposes of chemical evolution this gas is irrelevant since we assume it does not form stars, at least as long as it remains in the hot phase. Therefore, in this work we consider this gaseous component as effectively external to the galaxy and the metals present in it as lost.

In Fig. 5 (left-hand panel), we show the total observed mass of oxygen per unit area in stars (orange), in the ISM (violet), in ISM+stars (red) and the mass of metals that must have been produced by the observed stellar mass using our adopted yield (using

equation (8), blue line) as a function of radius. In the case of the ISM and ISM+stars lines, we show the results obtained with both the M08 (solid) and PP04 (dashed) metallicity calibrations. The error bars represent the error in the mean in each annulus, added in quadrature to the median of the intrinsic error in each of the physical quantities. The intrinsic error budget is dominated by the error on the stellar metallicity, followed by the uncertainty in metallicity and stellar mass (for both we get a median error of about 0.1 dex). These errors do not attempt to incorporate systematic effects, which would dominate the uncertainty budget for this study. Moreover, we take the net yield (y) and the return fraction (R) to be known exactly. With these caveats, Fig. 5 demonstrates that using the fiducial yield at all radii more metals have been produced than can be accounted for considering both the metals in the ISM and in stars.

In the discussion (Section 6), we argue that a different choice of IMF (adopting for example Salpeter or Chabrier IMF) only makes the metal deficit worse. We also note that the mass of metals in stars presents a sharp feature between 2.5 and 3 kpc, which is a direct consequence of the sharp feature in the stellar metallicity gradient. Since it is present in only one radial bin, the effect of this feature on the overall metal budget of the galaxy is negligible and will not be discussed further.

In Fig. 5, top right panel, we show the mass of oxygen in stars (orange) and ISM (violet) as a function of radius as a percentage of the total mass of oxygen produced in that annulus. The total mass of oxygen in each annulus (ISM + stars, red line) is also shown,

Table 3. The total oxygen mass in different galactic components, integrating the radial gradients for NGC 628 out to $R = 7.00$ kpc.

Metals	Mass [$10^7 M_{\odot}$]	Mass [% M_Z prod]
Stars	2.6 ± 0.9	$25 \pm 2\%$
ISM (M08)	3.2 ± 0.9	$31 \pm 3\%$
ISM (PP04)	2.3 ± 0.7	$23 \pm 2\%$
Stars + ISM (M08)	5.8 ± 1.7	$56 \pm 5\%$
Stars + ISM (PP04)	4.9 ± 1.5	$47 \pm 5\%$

and we plot the results using both the M08 (solid line) and PP04 (dot-dashed line) metallicity calibrations.

Fig. 5 (top-right) shows that the fraction of metals lost is about 45 per cent to 55 per cent, and approximately constant within the uncertainties for $R > 3$ kpc. There is also some evidence that the fraction of metals lost in the central region is higher (only ~ 30 per cent of the metals have been retained). This feature may trace the effect of massive outflows during the formation of the bulge or the cumulative effect of nuclear activity in the past. Interestingly, Fig. 5 (top-right) also shows that the fraction of metals retained increases at $R > 5$ kpc. Gas-phase metallicity measurements at even larger radii provided by the Berg et al. (2015) data set confirm and further extend this trend (see discussion in Section 6.2).

Fig. 5 (lower-right) shows the *cumulative* version of the previous plot. For each radius R , the mass of oxygen in different components *within* radius R is computed as a percentage of the mass of metals produced within the considered radius. This plot can be interpreted as the results that would be obtained for the integrated properties of NGC 628 if all quantities (metallicities, gas masses etc.) were measured using an aperture corresponding to a radius R on the sky.

We note that cumulatively the mass of oxygen in the ISM is sub-dominant out to $R \approx 5.5$ kpc, at the latter radius stars and ISM contribute roughly equally to the total oxygen budget. For easy reference, the masses of oxygen in the different components within 7.0 kpc are summarized in Table 3. Taking into account the uncertainty associated with the choice of metallicity calibration, we conclude that out to $R = 7.0$ kpc, the bulge and the disc of NGC 628 as a whole have lost ~ 50 per cent of the oxygen they have produced.

5.2 Inferred net outflow loading factor

As discussed above, in the absence of outflows the total amount of metals produced should be simply given by the stellar mass times the amount of metals produced per mass of long-lived stars (equation 8). To model the effect of outflows, we follow the formalism laid out in Peng & Maiolino (2014) and assume the outflow rate Ψ to be proportional to the SFR through a constant outflow loading factor λ ,

$$\Psi = \lambda \text{ SFR}. \quad (10)$$

The resulting total amount of metals is given by the equation

$$M_{Z(\text{tot})} = y M_{\star} - \lambda \int Z_g(t) \text{ SFR}(t) dt. \quad (11)$$

The last term is the ‘metal deficit’ and its evaluation requires knowledge of the evolution of the metallicity with the SFR. To make further progress, we therefore need to solve equations (1) and (2). A general solution as a function of time can be obtained assuming a star formation law. Following previous work, we use a simple linear relation of the form

$$\text{SFR} = \varepsilon M_{\text{gas}} \quad (12)$$

where ε is often referred to as the star formation efficiency or also as the inverse of the gas-depletion time ($1/\tau_d$).

The final piece of information needed is the functional form of gas-inflow rate Φ . A number of authors have assumed a gas-inflow rate proportional to the SFR (e.g. Matteucci & Chiosi 1983; Erb 2008; Mannucci et al. 2009; Dayal et al. 2013; Troncoso et al. 2014; Kudritzki et al. 2015). This assumption leads to simple analytical solutions of the resulting differential equations. Moreover, it does not require consideration of the time variable, since all the quantities evolve in time like the SFR and hence the time dependence factors out. However, the assumption of an inflow rate proportional to the SFR has no physical grounds and has been used in previous work entirely for convenience. A much more realistic assumption is that of a constant, or slowly varying, inflow rate. As discussed in Peng & Maiolino (2014), this assumption is much closer to the expectation based on the inflow rate of baryons in dark haloes inferred in analytical calculations and numerical simulations of structure formation (Faucher-Giguère, Kereš & Ma 2011; Dekel et al. 2013).

Interestingly, analytical solutions of equations (1)–(4) can still be obtained with the assumption of constant inflow rate, although they do depend explicitly on time. Exact solutions for M_g and M_{\star} are given in Peng & Maiolino (2014). Further exact solutions for Z_g and M_Z/M_{\star} are presented in Appendix A of this work. Here, we exploit those solutions to derive the relation between M_Z/M_{\star} and the gas fraction. We refer the interested reader to Appendix B for a detailed discussion of the assumptions, strengths and weaknesses of the different bathtub models and a justification of the choice made in this work.

We further show in appendix A that the relation between M_Z/M_{\star} and f_{gas} is *independent* of both the inflow rate and of star formation efficiency and depends only on the outflow loading factor. This is a very important point, since the relation between these two quantities is therefore a clear, non-degenerate tracer of the net effect of outflows (unlike the effective yield). The red lines in Fig. 6 show M_Z/M_{\star} as a function of f_{gas} , for different values of the outflow loading factor. Coloured symbols in Fig. 6 show the M_Z/M_{\star} and f_{gas} observed in different radial annuli in NGC 628, where the colour coding represents the radial distance from the galaxy centre. Filled symbols are for the M08 calibration, while hollow symbols are for the PP04 calibration. We note that this figure is just an alternative representation of the metal deficit discussed in the previous section (Fig. 5). Here, we have replaced the radial distance with f_{gas} , but the two quantities are related as discussed in Section 3.6, since the gas fraction increases monotonically with radius. The metal deficit can be visualized in Fig. 5 as the distance between the observational data points and the $\lambda = 0$ (solid red) line, which represents the $M_Z = y M_{\star}$ case.

By using the M08 calibration, the observed points are well reproduced with an outflow loading factor $\lambda \approx 1$, with a scatter in the range $0.5 < \lambda < 2$, except for the ‘anomalous’ point at 3 kpc, which requires a lower loading factor approaching zero. The PP04 calibration requires slightly higher loading factors (except again for the anomalous point at 3 kpc).

We emphasize that, since we use the *total* mass of metals relative to the mass of stars, our analysis provides an estimate of the *average* outflow loading factor during the galaxy lifetime, and not the current outflow rate in the galaxy. Indeed, within the picture of hierarchical formation of structure, it is possible that this average loading factor is mainly driven by the high efficiency of metal loss at higher redshift, when the physical condition in the galaxy and its sub-components would have been significantly different.

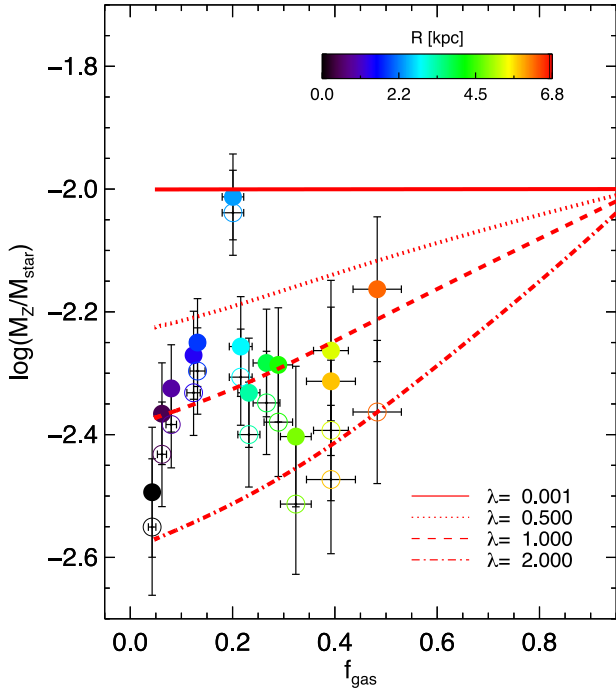


Figure 6. Metals-to-stellar mass ratio (M_Z/M_*) versus gas fraction (f_{gas}). Symbols show the values observed in radial annuli in NGC628, where the colour-coding gives the galactocentric radial distance, as indicated in the colour bar. Solid symbols correspond to the mass of metals in which the ISM metallicity is calculated by using the M08 calibration, while open symbols use the PP04 calibration. The red lines correspond to the prediction of simple chemical evolution models with different values for the average outflow loading factor λ . Note that the model relations are independent of the inflow rate Φ and of the star formation efficiency ε .

5.3 Modelling the gas metallicity

As shown in Appendix A, the chemical evolution framework adopted in the previous section also leads to a direct relation between gas metallicity (Z_g) and gas fraction (f_{gas}) that depends only on the outflow loading factor and not on the inflow rate and star formation efficiency. The relation between Z_g and f_{gas} has been studied by several authors, including recently Ascasibar et al. (2014) and Kudritzki et al. (2015), who extend their analysis to resolved scales making use of data from NGC 628.

However, unlike the metals locked in stars, the gas-phase metallicity is more subject to recent gas flow events (possible stochastic variations away from the ideal gas regulatory model), hence making it a less reliable tool for inferring the time-averaged properties of the system.

Keeping these caveats in mind, the model relations between Z_{gas} and f_{gas} are shown in Fig. 7, with the same outflow loading factors as in Fig. 6. The data points represent the observed values in NGC 628 and are colour-coded by radial distance. The two different metallicity calibrations are identified, as in Fig. 6, by solid (Maiolino et al. 2008) and hollow (Pettini & Pagel 2004) circles. The comparison of the models with the data points suggests outflow loading factors consistent with zero, or generally lower than those derived from the M_Z/M_* versus f_{gas} relation (Fig. 6).

We note that the mismatch applies (with about the same magnitude) both to the central regions, where the total mass of metals is dominated by the stellar component, and in the outer regions, where the total mass of metals is dominated by the gaseous component,

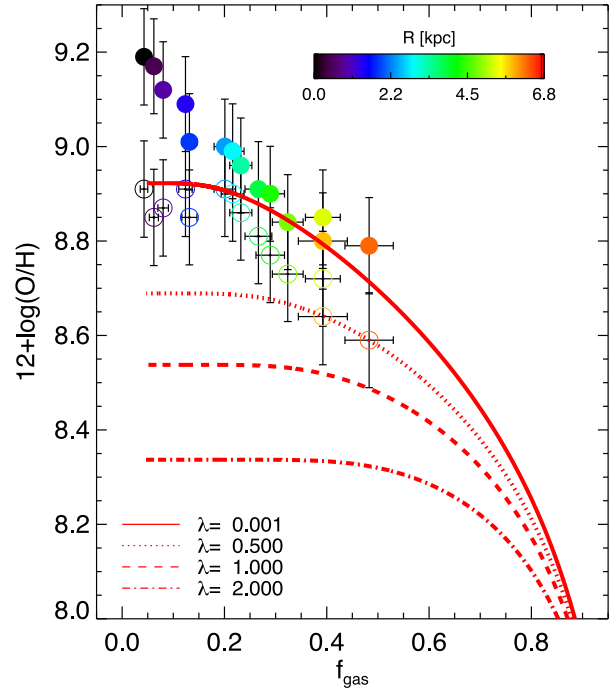


Figure 7. Gaseous metallicity $12 + \log(\text{O}/\text{H})$ versus gas fraction. Symbols show the values observed in radial annuli in NGC 628, where the colour-coding gives the galactocentric radial distance, as indicated in the colour bar. Solid symbols correspond to the mass of metals in which the ISM metallicity is calculated by using the M08 calibration, while open symbols use the PP04 calibration. The red lines correspond to the prediction of simple chemical evolution models with different values for the average outflow loading factor (λ). Note that the model relations are independent of the inflow rate Φ and of the star formation efficiency ε .

therefore, excluding that the mismatch is simply associated with a different metallicity scales or calibration issues associated with the calculation of one of the two quantities.

As discussed above, a possible solution can be attained assuming that the gas metallicity might not be representative of the average evolutionary processes during the life of the galaxy since it can be subject to recent galactic ‘weather’. In particular, a process that may strongly affect the gas metallicity, without significantly affecting the total content of metals, could be recent inflow of enriched gas from the halo. We discuss this option further in Section 6.

Finally we note that Kudritzki et al. (2015) have inferred a similarly low loading factor ($\lambda = 0.2\text{--}0.3$) for NGC 628, by fitting the gas-phase metallicity gradient and the gas fraction. Since they use T_e -based metallicities, their results should be compared with our analysis using the PP04 calibration, with which they are in qualitative agreement. However, Kudritzki et al. (2015) make use of a chemical evolution model where the inflow rate is proportional to the SFR. As discussed in Appendix B, this assumption introduces a dependence of the metallicity–gas fraction relation on the inflow rate, which is absent in our model.

6 DISCUSSION

In the previous section, we have demonstrated that (a) overall ~ 50 per cent of the oxygen produced by the NGC 628 out to $R = 7.0$ kpc is unaccounted for and (b) average outflow loading factors of order unity can explain the observed metal deficit, although there is a tension with the observed gas metallicity. While

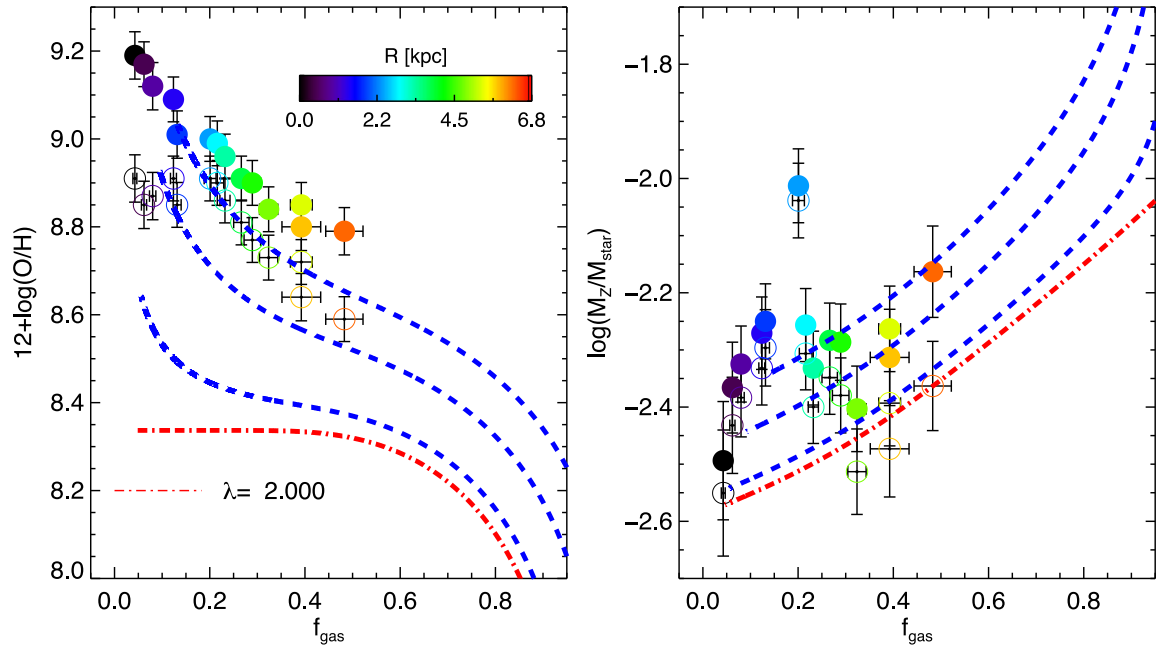


Figure 8. Same as Figs 6 and 7, but including a late time inflow of gas-rich material with metallicity $3Z_{\odot}$. The red line is the same as in Figs 6 and 7 and represents the model with $\lambda = 2$, while the blue lines represent an increasing mass of infalling metal-rich gas. Going upwards in both figures the blue lines represent an infalling metal-rich gas mass that is a fraction of 1 per cent, 5 per cent and 10 per cent of the mass of baryons already present in the disc at a given location.

we cannot entirely exclude that possibility that the tension is due to the unavoidable systematic uncertainties in the determination of gas phase and stellar metallicity and the choice of nucleosynthetic yield/IMF, in this section we discuss possible ways to interpret the discrepancy in light of different physical mechanisms.

6.1 Gas flows and disc–halo interaction

It is important to remember that the chemical evolution framework used in this work is an intentionally simple prescription. In particular, while the model allows metal-rich outflows and pristine gas inflows, and hence some exchange of gas and metals between the different radial bins, it does not treat the case of incoming metal-rich gas or changes in the stellar mass component due to stellar migration.

A number of physical processes, for example, might be responsible for funneling metal-rich gas into the central galactic regions, including viscous flows generated by gravitational instability or cloud–cloud collisions (Lacey & Fall 1985; Thon & Meusinger 1998; Ferguson & Clarke 2001) or the presence of a bar or other non-axisymmetric perturbation (Minchev & Famaey 2010; Matteo et al. 2013). The breaks seen in the stellar metallicity, and possibly the central flattening of the gas-phase metallicity profile when using the PP04 calibration, combined with the presence of a star formation ring just inside the break radius, may indeed support the hypothesis of an oval perturbation playing a role in the evolution of the disc in NGC 628.

More importantly, enriched gas expelled by previous generations of supernovae may fall back on to the disc, generating a galactic fountain. In the literature, however, there is no agreement on the details of the fountain mechanism (Melioli et al. 2008, 2009; Spitoni et al. 2010), the radial distance covered by a galactic fountain, the time needed for the gas to rain back on to the disc and the overall impact of this mechanism on the chemical abundances of the disc

itself. In hydrodynamical simulations, if a hot halo is present, metal-enriched gas can fall back towards the galactic centre (Melioli et al. 2009).

The presence of large amounts of metals in the halo of disc (and elliptical) galaxies has been inferred by recent *HST*-COS observations of absorption systems along the line of sight of background quasars (e.g. Tumlinson et al. 2011; Werk et al. 2014). However, these observations have probed the halo of galaxies at large radii (~ 100 kpc). In the inner region of the halo, the gas metallicity is not known observationally, but simulations expect that the metallicity of the diffuse gas should reach values higher than solar (Marinacci et al. 2014).

We have attempted to model an episode of metal-enriched accretion at late times by modifying the analytical description of the metallicity evolution discussed above with the introduction of an accreted enriched gas mass, proportional to the mass of baryons already present in the galaxy, and with a given metallicity $Z_{\text{gas-accr}}$. The blue lines in Fig. 8 show the effect of such a late enriched accretion by assuming that the accreted gas is 1, 5 and 10 per cent of the mass in baryons already present in the radial bin and that the metallicity of such enriched inflow is $Z_{\text{gas-accr}} = 3Z_{\odot}$ (which is consistent with the enrichment of the hot gas phase expected by some models, Marinacci et al. 2014). Clearly such a model can now broadly reproduce the trend of the gas metallicities in NGC 628 at several radii. At the same time, Fig. 8 illustrates that such a late enriched accretion has little effect on the total content of metals, hence having little effect on the global, average outflow rate that we have inferred from the metal deficit.

In these models, we have assumed an outflow loading factor $\lambda = 2.0$, i.e. higher than inferred in the previous section, to better illustrate that late enriched accretion can have a strong effect on the final gas metallicity but little effect on the total content of metals. We note that by starting with a lower loading factor (e.g. $\lambda = 1.0$), the enriched inflow can reproduce the data with a smaller amount of accreted gas (~ 3 –5 per cent).

Both gas flows in the disc and galactic fountains might therefore help resolve the tension between the metal deficit and the outflow loading factor implied from the gas-phase metallicity for the central regions of NGC 628 by increasing the metallicity of the central regions beyond what is expected in the absence of these metal-rich inflows. We note that there is a fundamental degeneracy in this type of model between the outflow loading factor and the mass (and metallicity) of the enriched inflow when using the gas-phase metallicity alone. However, better constraints can be derived if one models, as we do here, both the stellar and the gas-phase metallicity at the same time, because the gas-phase metallicity is largely independent of gas flows at late times.

Stellar migration (Roskar et al. 2008b; Yoachim, Roškar & Debattista 2012; Spitoni et al. 2015) might also play a role in alleviating the observed tension. If stars diffuse out of the radial bin in which they are born, we would be making incorrect inferences for the gas fraction and oxygen mass in the bin. We can model this effect naively by considering that the observed stellar mass in each bin should be corrected for the net effect of migration. We experimented with this prescription and found that changes in the stellar mass up to 0.3 dex only generate small changes in M_Z/M_* for all bins within $R = 5$ kpc, since the metal budget is dominated by the stellar component and therefore M_Z/M_* is only weakly dependent on stellar mass. At larger radial distances the oxygen mass budget is dominated by the ISM and the effect of changing the stellar mass content is larger. If a large fraction of the stellar mass currently observed at large radii is the result of stellar migration from the centre, we would require a lower outflow loading factor in the outer disc, going towards a reduction of the tension between the metal deficit and the observed gas metallicity.

6.2 Towards larger galactocentric distances

The behaviour of the metal budget at even larger radii than the ones probed by our investigation constitutes a particularly interesting avenue for future work. Since H I discs extend substantially more than the stellar component, low levels of chemical enrichment in the outer disc might mean that a large fraction of metals have escaped our budget. Unfortunately, there is no consensus in the literature on the nature of the metallicity gradient for $R > 2R_c$. While Bresolin et al. (2012) and Sánchez et al. (2014) argue for a flattening of the gradient beyond $R = 2R_c$, Moran et al. (2012) observed a sharp drop in the metallicity gradient for a subset of H I-rich galaxies.

Direct measurements of the chemical abundances at large galactocentric radii have been recently obtained for NGC 628 by Berg et al. (2015). Their observations contain 12 H II regions at radii larger than those sampled by the IFS data presented in this work. With the very scarce and scattered available data, there is no evidence for either a flattening or a break in the metallicity gradient of NGC 628 out to 10 kpc. These observations are interesting in the context of the metal budget because they confirm the trend that regions at large galactocentric distances have retained a larger fraction of their metals compared to the inner regions of galaxies. In particular, relying on the metallicity gradient reported in Berg et al. (2015), we conclude that the radial bin around 10 kpc has retained ~ 80 – 100 per cent of the metals produced *in situ*.

Intriguingly, previous work has also presented evidence that H II regions at extreme galactocentric distances ($R > R_{24} \approx 3R_c$) are more metal rich than expected from *in situ* star formation (Bresolin et al. 2009, 2012). These observations might be consistent with an extrapolation of the trend discussed above and in general with the idea that gas rich, relatively un-evolved systems have a smaller

metal deficit, or might even have acquired metals through enriched inflows from the central regions (through a galactic fountain). In the context of inside-out disc growth, these outer regions are still in the process of assembly and thus represent an ideal laboratory to study disc formation as it happens.

6.3 The effect of the IMF and the nucleosynthetic yield

In this work, we have used the Kroupa et al. (1993) IMF, since this is the IMF which fits best the chemical evolution of galaxy discs (Romano et al. 2005, 2010). A different IMF would have an impact on our calculations by implying a different population-averaged net yield, since different elements are produced by stars of different masses. In this section, we briefly discuss the implications of adopting different IMFs.

A Salpeter IMF would give a significantly higher metal deficit, implying a loss of about 75 per cent of the metals produced. The inferred average loading factor would be about $\lambda \sim 2$ – 4 . In the case of a Chabrier (2003) IMF, the metal deficit is even more severe: more than 85 per cent of the metals should be lost and in the implied average loading factor should be in the range $\lambda > 5$. The Kroupa (2001) IMF gives results very similar to Chabrier (2003). We note that in going from a Kroupa to a Salpeter IMF we correct the stellar mass profile by a factor of 0.26 dex.

Such large loading factors are extreme, especially considering that these are loading factors averaged during the lifetime of the galaxy, and have never been seen in galactic winds studies locally or even in high- z galaxy discs (e.g. Steidel et al. 2010; Genzel et al. 2011), which instead infer outflow loading factors more in line with the results obtained by using the Kroupa et al. (1993) IMF, further confirming that this IMF is the most appropriate for modelling galaxy discs.

However, it has been pointed out that the chemical properties of spheroids (including bulges) may be more accurately described by a Chabrier (2003) IMF. If we apply the latter IMF only to the central region, we get a large metal deficit (~ 90 per cent) for the bulge. This would be in line with similar estimates for the Milky Way, according to which the bulge of our Galaxy has lost about 80 per cent of its metals (Greggio & Renzini 2011). The Chabrier (2003) IMF applied to the central region would also imply a central outflow loading factor of about $\lambda \sim 5$. Since we are only measuring the time-averaged outflow loading factor, it is not implausible to find that the central regions of galaxies have experienced stronger outflows, despite the fact that at present time they sit at the bottom of the galaxy's potential well. Indeed outflow rates with such large loading factor are observed in the central region of local and high- z galaxies (Feruglio et al. 2010; Rupke & Veilleux 2011; Maiolino et al. 2012; Cicone et al. 2014, 2015), and may be explained with the additional boost to the outflow rate associated with quasar-driven winds or with extreme nuclear starbursts in the past, when these feedback processes were likely more violent than in the present Universe.

6.4 The oxygen deficit in context

Previous work has estimated the oxygen (or metal) budget in star-forming disc galaxies by statistical arguments, making use of scaling relations (between mass and SFR, between gas fraction and stellar mass, and between mass and metallicity) demonstrated to hold in large samples of galaxies observed spectroscopically (Bouché et al. 2007; Zahid et al. 2012; Peebles et al. 2014). These works predict an oxygen deficit ranging from 35 per cent to 90 per cent, with large

statistical uncertainties, related both to the intrinsic scatter in the scaling relations used as input for the models and to the difficulty to robustly correct for aperture effects. Nonetheless it is rewarding to note that our estimate for the metal deficit in NGC 628 falls inside the range of estimates from previous works.

Due to the difficulty of studying the stellar metallicity and thus deriving the total metal content in galaxies, the relation between gas-phase metallicity and gas fraction has been widely used as an observationally more accessible tool to investigate the impact of outflows. Recent work (Dayal, Ferrara & Dunlop 2013; Lilly et al. 2013; Ascasibar et al. 2014; Lu, Blanc & Benson 2015) generally agrees on loading factors of order unity for galaxies of stellar mass $\log(M_*/M_\odot) \sim 10$.

Extending this study to a larger sample of galaxies with resolved gas masses and metallicity information would provide the logical way forward to studying the effect of outflows across the whole galaxy population and uncover trends with galaxy parameters (stellar mass, SFR etc.). In particular, low-mass galaxies ($\log(M_*/M_\odot) < 9$) are predicted to exhibit higher outflow loading factors in order to match their low observed baryon fractions (McGaugh et al. 2010), their metallicity (Lu et al. 2015) and to reconcile the faint-end slopes of the dark matter and galaxy mass functions (Lilly et al. 2013). Some observational evidence for higher outflow rates in dwarf starbursts can be found in the literature (e.g. Martin, Kobulnicky & Heckman 2002), but more evidence in this mass regime is urgently needed.

While such a programme is observationally costly, the synergy between large IFS surveys (CALIFA, SAMI and MaNGA) and radio and sub-mm interferometers (ALMA, NOEMA, JVLA) will greatly increase the availability of matched-resolution data sets to use for this type of study in the near future.

6.5 A link between outflows and baryon fraction

The metal deficit is tightly related to the well-known ‘missing baryon problem’ (e.g. Fukugita, Hogan & Peebles 1998; McGaugh et al. 2010; Shull et al. 2012). Within our ‘baryon cycling’ framework we cannot account for the inventory of cosmic baryons, a large fraction of which are believed to exist in the IGM and CGM. However, within the gas regulatory model, outflows modulate the final baryonic mass of the system, while the gas-inflow rate can be assumed to be directly proportional to the dark matter halo mass growth rate. Peng & Maiolino (2014) provide a useful parametrization to relate the halo mass (M_h) and the gas-inflow rate (Φ)

$$\Phi = f_b f_{\text{gal}} \frac{dM_h}{dt}, \quad (13)$$

where $f_b = 0.155$ (Planck Collaboration XVI 2014) is the cosmic baryon fraction and f_{gal} is the fraction of accreting baryons that penetrates into the inner galaxy disc, which could be a complex function of halo mass and redshift. Relying on results from the hydrodynamical simulations in Dekel et al. (2013), we follow Peng & Maiolino (2014) and assume for simplicity $f_{\text{gal}} \sim 0.5$ in this section.

The evolution of the total baryonic content of the system ($M_b = M_g + M_*$) is dictated by equations (1) and (2) so that $dM_b/dt = \Psi - \Phi$. Combining this with equation (13) we obtain

$$M_b = f_b f_{\text{gal}} M_h - \frac{\lambda}{1-R} M_*. \quad (14)$$

Rearranging we finally obtain a relation between gas fraction (f_{gas}), outflow loading factor (λ) and the detected baryon fraction

($f_d \equiv \frac{M_b}{f_b M_h}$, as defined in McGaugh et al. 2010)

$$f_d \equiv \frac{M_b}{f_b M_h} = f_{\text{gal}} \left(1 + \frac{\lambda}{(1-R)(1+f_{\text{gas}})} \right)^{-1}. \quad (15)$$

Using representative values for NGC 628, $f_{\text{gas}} = 0.2$ and $\lambda = 1$, we obtain $f_d \sim 0.23$. This very rough order-of-magnitude calculation leads to a detected baryon fraction that is surprisingly close to the detected baryons fractions measured via the Tully–Fisher relation in McGaugh et al. (2010), who quote $f_d \sim 0.16 - 0.19$ for disc galaxies of stellar mass $\log(M_*/M_\odot) = 9.9-10.1$, comparable to NGC 628.

7 CONCLUSIONS

In this work, we have presented a detailed study of the metal content and distribution in the nearby disc galaxy NGC 628. We have mapped the gas-phase metallicity by exploiting the largest IFS mosaic available to date, thus enabling us to extend our study out to a galactocentric radius of 7 kpc ($\sim 3 R_c$). We have combined the gas metallicity map with the stellar metallicity radial profile presented in previous work (Sánchez-Blázquez et al. 2014), the stellar mass surface density distribution Σ_* (inferred from extensive multi-band photometry) and the observed gas surface density ($\Sigma_{\text{H I}}$, Σ_{H_2}) inferred from CO and H I maps.

By comparing the mass of metals observed in the gaseous and stellar components with the mass of metals produced by stars in the same region (inferred assuming the latest determination of the oxygen nucleosynthetic yield, Vincenzo et al. 2015), we have obtained a detailed, spatially resolved metal budget as function of galactocentric radius. The main results from this analysis are the following.

(i) On average about 50 per cent of the metals produced by the stars in each galactic region have been lost. The fraction of metals lost is higher (~ 70 per cent) in the central region, which is dominated by the bulge. There is also tentative indication that the fraction of metals lost decreases at large galactocentric radii. Cumulatively, out to a radius of 7 kpc, 45–50 per cent of the *total* amount of metals produced have been lost by the galaxy. Evidence from recent measurements of outlying H II regions from Berg et al. (2015) (out to 10 kpc) confirms the trend that regions in the outer disc have retained a higher fraction of the metals they have produced, with regions at around 10 kpc retaining $\sim 80-100$ per cent of the metals produced there.

(ii) We have used simple (‘bathtub’ and ‘gas regulatory’) analytical models involving gas outflow and inflow to model the data. In this framework, the relation between metals-to-stellar mass ratio (M_z/M_{star}) and gas fraction (f_{gas}) is independent of the inflow rate and of the efficiency of star formation, and depends only on the outflow loading factor in models with constant inflow rate. We find that an outflow loading factor $\lambda \approx 1$ can explain the data at most radii, though with large scatter ($0.5 < \lambda < 2$). We emphasize that, since this inference is based on the total metal budget, we derive a time-averaged outflow rate, representative of the strength of outflows over the lifetime of the galaxy. This information is thus complementary to that obtained in studies based on the observed gas kinematics, which are sensitive only to the ongoing/recent outflow activity.

(iii) A larger loading factor may be derived if we make use of the Chabrier IMF. This IMF might be relevant for the central spheroid, thus implying a higher outflow rate during the early formation of the bulge.

(iv) The gas-phase metallicity is more sensitive to recent evolutionary processes because it is associated with a component of

the galaxy (the ISM) that is potentially subject to rapid evolution. We find that the observed gas metallicity cannot be reproduced by the same parameters inferred from the metal budget, independently from the choice of metallicity calibrator used. In particular, the observed gas-phase metallicities would require little or no outflow. We show that the apparent tension could be explained with infall of enriched gas from the halo at late times. Indeed, such a process would strongly affect the observed gas metallicity, but not the total mass of metals.

(v) Finally, we warn against the use of analytical models in which the inflow rate is assumed to be proportional to the SFR. This assumption, adopted in previous work, is not physically motivated and introduces an unnecessary degeneracy between inflow and outflow rates when modelling chemical abundances. Analytical solutions are presented in this work for models assuming a constant, or slowly varying, accretion rate, which is a much better representation of gas inflows in the cosmological framework. However, further work is needed to reliably test the validity of the underlying assumptions of the simple regulatory model presented in this work for describing regions within galaxies.

ACKNOWLEDGEMENT

FB acknowledges support from the United Kingdom Science and Technology Facilities Council. This work makes use of THINGS ('The Nearby Galaxy Survey', Walter et al. 2008), HERACLES (the 'HERA CO line Extragalactic Survey', Leroy et al. 2009) and PINGS (the 'PPAK IFS Nearby Galaxy Survey', Rosales-Ortega et al. 2010). We acknowledge the contribution from the referee in improving the content and the clarity of the paper. We thank Fiorenzo Vincenzo and Francesca Matteucci for their invaluable help in interpreting the vast literature on chemical abundance modelling and nucleosynthetic yields. We also thank Ying-jie Peng for support and discussion on development of his chemical evolution models. We wish to thank Fabian Rosales-Ortega for kindly sharing the PINGS data on NGC 628 and for his encouragement and feedback on the early stages of this work. We thank Matt Auger for useful discussions and healthy skepticism.

REFERENCES

Abazajian K. N. et al., 2009, *ApJS*, 182, 543
 Abdo A. A. et al., 2010, *AJ*, 710, 133
 Andrews B. H., Martini P., 2013, *AJ*, 765, 140
 Aniano G., Draine B. T., Gordon K. D., Sandstrom K., 2011, *PASP*, 123, 1218
 Arribas S., Colina L., Bellocchi E., Maiolino R., Villar-Martin M., 2014, *A&A*, 568, A14
 Ascasibar Y., Gavil M., Pinto N., Casado J., Rosales F., 2014, *MNRAS*, 448, 2126
 Asplund M., Grevesse N., Sauval A. J., Scott P., 2009, *ARA&A*, 47, 481
 Baldwin J. A., Phillips M. M., Terlevich R., 1981, *PASP*, 93, 5
 Belfiore F. et al., 2015, *MNRAS*, 449, 867
 Bell E. F., de Jong R. S., 2001, *AJ*, 550, 212
 Bell E. F., McIntosh D. H., Katz N., Weinberg M. D., 2003, *ApJS*, 149, 289
 Berg D. A., Croxall K. V., Skillman E. D., Pogge R. W., Moustakas J., Groh-Johnson M., 2015, *ApJ*, 806, 1
 Binette L., Matadamas R., Hägele G. F., Nicholls D. C., Magris G. C., 2012, *A&A*, 547, A29
 Blanc G. A. et al., 2013, *AJ*, 764, 117
 Blanc G. A., Kewley L., Vogt F. P. A., Dopita M. A., 2015, *AJ*, 798, 99
 Boissier S., Prantzos N., 1999, *MNRAS*, 307, 857
 Bolatto A. D., Wolfire M., Leroy A. K., 2013, *ARA&A*, 51, 207
 Boquien M. et al., 2012, *A&A*, 539, A145
 Bouché N., Lehnert M. D., Aguirre A., Peroux C., Bergeron J., 2007, *MNRAS*, 378, 525

Bregman J. N., Miller E. D., Seitzer P., Cowley C. R., Miller M. J., 2013, *AJ*, 766, 57
 Bresolin F., 2007, *AJ*, 656, 186
 Bresolin F., Ryan-Weber E., Kennicutt R. C., Goddard Q., 2009, *AJ*, 695, 580
 Bresolin F., Kennicutt R. C., Ryan-Weber E., 2012, *AJ*, 750, 122
 Bundy K. et al., 2015, *AJ*, 798, 7
 Burgarella D., Buat V., Iglesias-Páramo J., 2005, *MNRAS*, 360, 1413
 Calzetti D., 2001, *PASP*, 113, 1449
 Cano-Díaz M., Maiolino R., Marconi A., Netzer H., Shemmer O., Cresci G., 2012, *A&A*, 537, L8
 Cappellari M., Emsellem E., 2004, *PASP*, 116, 138
 Cardelli J. A., Clayton G. C., Mathis J. S., 1989, *AJ*, 345, 245
 Cavichia O., Molla M., Costa R. D. D., Maciel W. J., 2013, *MNRAS*, 437, 3688
 Cazzoli S., Arribas S., Colina L., Bellocchi E., Emonts B., Maiolino R., 2014, *A&A*, 569, A14
 Chabrier G., 2003, *PASP*, 115, 763
 Cicone C. et al., 2014, *A&A*, 562, A21
 Cicone C. et al., 2015, *A&A*, 574, A14
 Cid Fernandes R., Stasiska G., Mateus a., Vale Asari N., 2011, *MNRAS*, 413, 1687
 Cid Fernandes R. et al., 2014, *A&A*, 561, A130
 Colavitti E., Cescutti G., Matteucci F., Murante G., 2009, *A&A*, 496, 429
 Croom S. M. et al., 2012, *MNRAS*, 421, 872
 Croxall K. V. et al., 2013, *AJ*, 777, 96
 Davé R., Finlator K., Oppenheimer B. D., 2011, *MNRAS*, 421, 98
 Dayal P., Ferrara a., Dunlop J. S., 2013, *MNRAS*, 430, 2891
 Dekel A., Mandelker N., 2014, *MNRAS*, 444, 2071
 Dekel A., Zolotov A., Tweed D., Cacciato M., Ceverino D., Primack J. R., 2013, *MNRAS*, 435, 999
 Denicolo G., Terlevich R., Terlevich E., 2002, *MNRAS*, 330, 69
 Dopita M. A., Sutherland R. S., Nicholls D. C., Kewley L. J., Vogt F. P. A., 2013, *ApJS*, 208, 10
 Edmunds M. G., 1990, *MNRAS*, 246, 678
 Erb D. K., 2008, *AJ*, 674, 151
 Faucher-Giguère C. A., Kereš D., Ma C. P., 2011, *MNRAS*, 417, 2982
 Fazio G. G. et al., 2004, *ApJS*, 154, 10
 Ferguson A. M. N., Clarke C. J., 2001, *MNRAS*, 325, 781
 Fernandes R. C., Sodri L., Gomes M., 2005, *MNRAS*, 358, 363
 Ferrara A., Scannapieco E., Bergeron J., 2005, *AJ*, 634, L37
 Feruglio C., Maiolino R., Piconcelli E., Menci N., Aussel H., Lamastra A., Fiore F., 2010, *A&A*, 518, L155
 Fukugita M., Hogan C. J., Peebles P. J. E., 1998, *ApJ*, 503, 518
 Gallazzi A., Charlot S., Brinchmann J., White S. D. M., 2006, *MNRAS*, 370, 1106
 Garnett D. R., 1992, *AJ*, 103, 1330
 Genzel R. et al., 2011, *AJ*, 733, 101
 Gibson B. K., Fenner Y., Renda A., Kawata D., Lee H.-c., 2003, *PASA*, 20, 401
 González Delgado R. M. et al., 2013, *A&A*, 562, A47
 Greggio L., Renzini A., 2011, *Stellar Populations. A User Guide from Low to High Redshift*. Wiley-VCH Verlag GmbH & Co. KGaA
 Heavens A., Jimenez R., Lahav O., 2000, *MNRAS*, 317, 965
 Heckman T. M., Lehnert M. D., Strickland D. K., Armus L., 2000, *ApJS*, 129, 493
 Izotov Y. I., Stasiska G., Meynet G., Guseva N. G., Thuan T. X., 2006, *A&A*, 448, 955
 Kamphuis J., Briggs F., 1992, *A&A*, 253, 335
 Kauffmann G. et al., 2003, *MNRAS*, 346, 1055
 Kelz A. et al., 2006, *PASP*, 118, 129
 Kewley L. J., Dopita M. A., 2002, *ApJS*, 142, 35
 Kewley L. J., Ellison S. L., 2008, *AJ*, 681, 1183
 Kewley L. J., Dopita M. A., Sutherland R. S., Heisler C. A., Trevena J., 2001, *AJ*, 556, 121
 Kobayashi C., Umeda H., Nomoto K., Tominaga N., Ohkubo T., 2006, *AJ*, 653, 1145
 Kobulnicky H. A., Kewley L. J., 2004, *AJ*, 617, 240
 Kroupa P., 2001, *MNRAS*, 322, 231

- Kroupa P., Tout C. A., Gilmore G., 1993, *MNRAS*, 262, 545
- Kudritzki R.-P., Ho I.-T., Schruba A., Burkert A., Zahid H. J., Bresolin F., Dima G. I., 2015, *MNRAS*, 450, 342
- Lacey C. G., Fall S. M., 1985, *AJ*, 290, 154
- Le Borgne J.-F. et al., 2003, *A&A*, 402, 433
- Leroy A. K. et al., 2009, *AJ*, 137, 4670
- Leroy A. K. et al., 2012, *AJ*, 144, 3
- Lilly S. J., Carollo C. M., Pipino A., Renzini A., Peng Y., 2013, *AJ*, 772, 119
- López-Sánchez A. R., Dopita M. A., Kewley L. J., Zahid H. J., Nicholls D. C., Scharwächter J., 2012, *MNRAS*, 426, 2630
- Lu Y., Blanc G. A., Benson A., 2015, *AJ*, 808, 129
- Maiolino R. et al., 2008, *A&A*, 488, 463
- Maiolino R. et al., 2012, *MNRAS*, 425, L66
- Mannucci F. et al., 2009, *MNRAS*, 398, 1915
- Mannucci F., Cresci G., Maiolino R., Marconi A., Gnerucci A., 2010, *MNRAS*, 408, 2115
- Maraston C., 2005, *MNRAS*, 362, 799
- Maraston C., Stromback G., 2011, *MNRAS*, 418, 2785
- Marcon-Uchida M. M., Matteucci F., Costa R. D. D., 2010, *A&A*, 520, A35
- Marinacci F., Pakmor R., Springel V., Simpson C. M., 2014, *MNRAS*, 442, 3745
- Marino R. A. et al., 2013, *A&A*, 559, A114
- Martin C. L., 2005, *AJ*, 621, 227
- Martin C. L., 2006, *AJ*, 647, 222
- Martin C., Kobulnicky H., Heckman T., 2002, *ApJ*, 574, 663
- Matteo P. D., Haywood M., Combes F., Semelin B., Snaith O. N., 2013, *A&A*, 553, A102
- Matteucci F., 1986, *PASP*, 98, 973
- Matteucci F., Chiosi C., 1983, *A&A*, 123, 121
- Matteucci F., Francois P., 1989, *MNRAS*, 239, 885
- McDermid R. M. et al., 2015, *MNRAS*, 448, 3484
- McGaugh S. S., Schombert J. M., de Blok W. J. G., Zagursky M. J., 2010, *ApJ*, 708, L14
- Melioli C., Brighenti F., D’Ercole A., de Gouveia Dal Pino E. M., 2008, *MNRAS*, 388, 573
- Melioli C., Brighenti F., D’Ercole a., de Gouveia Dal Pino E. M., 2009, *MNRAS*, 399, 1089
- Minchev I., Famaey B., 2010, *AJ*, 722, 112
- Moran S. M. et al., 2012, *AJ*, 745, 66
- Morrissey P. et al., 2007, *ApJS*, 173, 682
- Moustakas J., Kennicutt R. C., Tremonti C. A., Dale D. A., Smith J.-D. T., Calzetti D., 2010, *ApJS*, 190, 233
- Naab T., Ostriker J. P., 2006, *MNRAS*, 366, 899
- Nagao T., Maiolino R., Marconi A., 2006, *A&A*, 459, 85
- Nicholls D. C., Dopita M. A., Sutherland R. S., Kewley L. J., Palay E., 2013, *ApJS*, 207, 21
- Noll S., Burgarella D., Giovannoli E., Buat V., Marcellac D., Muñoz Mateos J. C., 2009, *A&A*, 507, 1793
- O’Donnell J. E., 1994, *AJ*, 422, 158
- Oppenheimer B. D., Davé R., 2006, *MNRAS*, 373, 1265
- Oppenheimer B. D., Davé R., Katz N., Kollmeier J. A., Weinberg D. H., 2012, *MNRAS*, 420, 829
- Osterbrock D. E., Ferland G. J., 2006, *Astrophysics of Gaseous Nebulae and Active Galactic Nuclei*. University Science Books, Mill Valley, CA
- Pagel B. E. J., Simonson E. A., Terlevich R. J., Edmunds M. G., 1992, *MNRAS*, 255, 325
- Panther B., Heavens A. F., Jimenez R., 2004, *MNRAS*, 355, 764
- Peebles M. S., Shankar F., 2011, *MNRAS*, 417, 2962
- Peebles M. S., Werk J. K., Tumlinson J., Oppenheimer B. D., Prochaska J. X., Katz N., Weinberg D. H., 2014, *AJ*, 786, 54
- Peimbert A., Peimbert M., 2010, *AJ*, 724, 791
- Peña Guerrero M. a., Peimbert A., Peimbert M., 2012, *AJ*, 756, L14
- Peng Y., Maiolino R., Cochrane R., 2015, *Nature*, 521, 192
- Peng Y.-j., Maiolino R., 2014, *MNRAS*, 443, 3643
- Pérez-Montero E., 2014, *MNRAS*, 441, 2663
- Pérez-Montero E., Contini T., 2009, *MNRAS*, 398, 949
- Pettini M., Pagel B. E. J., 2004, *MNRAS*, 348, L59
- Pettini M., Ellison S. L., Steidel C. C., Bowen D. V., 1999, *AJ*, 510, 576
- Pilkington K. et al., 2012, *A&A*, 540, A56
- Pilyugin L. S., Thuan T. X., 2005, *AJ*, 631, 231
- Pilyugin L. S., Vílchez J. M., Thuan T. X., 2010, *AJ*, 720, 1738
- Planck Collaboration XVI, 2014, *A&A*, 571, A16
- Romano D., Chiappini C., Matteucci F., Tosi M., 2005, *A&A*, 430, 491
- Romano D., Karakas A. I., Tosi M., Matteucci F., 2010, *A&A*, 522, A32
- Rosales-Ortega F. F., Kennicutt R. C., Sánchez S. F., Díaz a. I., Pasquali A., Johnson B. D., Hao C. N., 2010, *MNRAS*, 405, 735
- Rosales-Ortega F. F., Díaz a. I., Kennicutt R. C., Sánchez S. F., 2011, *MNRAS*, 415, 2439
- Roskar R., Debattista V. P., Stinson G. S., Quinn T. R., Kaufmann T., Wadsley J., 2008a, *AJ*, 675, L65
- Roskar R., Debattista V. P., Quinn T. R., Stinson G. S., Wadsley J., 2008b, *AJ*, 684, L79
- Rupke D. S. N., Veilleux S., 2011, *ApJ*, 729, L27
- Sanchez S., Rosales-Ortega F., Kennicutt R. C., Johnson B. D., Diaz A. I., Pasquali A., Hao C. N., 2011, *MNRAS*, 410, 313
- Sánchez S. F. et al., 2012, *A&A*, 538, A8
- Sánchez S. F. et al., 2014, *A&A*, 563, A49
- Sánchez-Blázquez P., Ocvirk P., Gibson B. K., Pérez I., Peletier R. F., 2011, *MNRAS*, 415, 709
- Sánchez-Blázquez P., Rosales-Ortega F., Diaz A., Sanchez S. F., 2014, *MNRAS*, 437, 1534
- Scannapieco C., Tissera P. B., White S. D. M., Springel V., 2006, *MNRAS*, 371, 1125
- Schruba A. et al., 2011, *AJ*, 142, 37
- Searle L., Sargent W. L. W., 1972, *ApJ*, 173, 25
- Shen S., Wadsley J., Stinson G., 2010, *MNRAS*, 407, 1581
- Shull J. M., Smith B. D., Danforth C. W., 2012, *AJ*, 759, 23
- Skrutskie M. F. et al., 2006, *AJ*, 131, 1163
- Solomon P. M., Rivolo A. R., Barrett J., Yahil A., 1987, *AJ*, 319, 730
- Spitoni E., Matteucci F., 2011, *A&A*, 531, A72
- Spitoni E., Calura F., Matteucci F., Recchi S., 2010, *A&A*, 514, A73
- Spitoni E., Romano D., Matteucci F., Ciotti L., 2015, *ApJ*, 802, 129
- Stasinska G., 2005, *A&A*, 434, 507
- Steidel C. C., Erb D. K., Shapley A. E., Pettini M., Reddy N., Bogosavljević M., Rudie G. C., Rakic O., 2010, *AJ*, 717, 289
- Strong A. W., Mattox J. R., 1996, *A&A*, 308, L21
- Sturm E. et al., 2011, *ApJ*, 733, L16
- Thomas D., Greggio L., Bender R., 1998, *MNRAS*, 296, 119
- Thon R., Meusinger H., 1998, *A&A*, 338, 413
- Tremonti C. A., Heckman T. M., Kauffmann G., Brinchmann J., White S. D. M., Seibert M., Peng E. W., Schlegel D. J., 2004, *AJ*, 613, 898
- Tremonti C. A., Moustakas J., Diamond-Stanic A. M., 2007, *AJ*, 663, L77
- Troncoso P. et al., 2014, *A&A*, 563, A58
- Tumlinson J. et al., 2011, *Science*, 334, 948
- Tumlinson J. et al., 2013, *AJ*, 777, 59
- Veilleux S., Osterbrock D. E., 1987, *ApJS*, 63, 295
- Veilleux S., Cecil G., Bland-Hawthorn J., 2005, *ARA&A*, 43, 769
- Vila-Costas M. B., Edmunds M. G., 1992, *MNRAS*, 259, 121
- Vincenzo F., Matteucci F., Belfiore F., Maiolino R., 2015, preprint ([arXiv:1503.08300v1](https://arxiv.org/abs/1503.08300v1))
- Walter F., Brinks E., Blok W. J. G. D., Bigiel F., Kennicutt R. C., Thornley M. D., Leroy A., 2008, *AJ*, 136, 2563
- Werk J. K., Prochaska J. X., Thom C., Tumlinson J., Tripp T. M., O’Meara J. M., Peebles M. S., 2013, *ApJS*, 204, 17
- Werk J. K. et al., 2014, *AJ*, 792, 8
- Wiersma R. P. C., Schaye J., Theuns T., 2011, *MNRAS*, 415, 353
- Wilkinson D. M. et al., 2015, *MNRAS*, 449, 328
- Williams B. F., Dalcanton J. J., Dolphin A. E., Holtzman J., Sarajedini A., 2009, *ApJ*, 695, L15
- Worthey G., Faber S. M., Gonzalez J. J., Burstein D., 1994, *ApJS*, 94, 687
- Yan R., Blanton M. R., 2012, *AJ*, 747, 61
- Yoachim P., Roškar R., Debattista V. P., 2012, *AJ*, 752, 97
- York D. G. et al., 2000, *AJ*, 120, 1579
- Zahid H. J., Dima G. I., Kewley L. J., Erb D. K., Davé R., 2012, *AJ*, 757, 54

Table A1. Exact analytical time-dependent solution of the Peng & Maiolino (2014) models with constant inflow rate for different galaxy properties. The equilibrium timescale τ is defined in equation (A1).

Galaxy property	Exact solution	$t \ll \tau$	$t \gg \tau$
M_g	$\Phi \tau (1 - e^{-t/\tau})$	Φt	$\Phi \tau$
$\text{SFR} = \varepsilon M_g$	$\varepsilon \Phi \tau (1 - e^{-t/\tau})$	$\varepsilon \Phi t$	$\varepsilon \Phi \tau$
M_\star	$\Phi \tau^2 \varepsilon (1 - R) (t/\tau - (1 - e^{-t/\tau}))$	$\Phi \varepsilon (1 - R) t^2/2$	$\Phi \varepsilon (1 - R) \tau t$
$f_{\text{gas}} \equiv \frac{M_g}{M_g + M_\star}$	$\left[1 + \varepsilon \tau (1 - R) \left(\frac{t}{\tau} \frac{1}{1 - e^{-t/\tau}} - 1 \right) \right]^{-1}$	$(1 + \varepsilon (1 - R) t/2)^{-1}$	$(1 + \varepsilon (1 - R) t)^{-1}$
$Z_g \equiv M_{Z_g}/M_g$	$p \varepsilon \tau \left(1 - \frac{t/\tau e^{-t/\tau}}{1 - e^{-t/\tau}} \right)$	$p \varepsilon t/2$	$p \varepsilon \tau$
M_Z	$p \varepsilon \Phi \tau^2 [(1 - \varepsilon \lambda t)(t/\tau - (1 - e^{-t/\tau})) - \varepsilon \lambda t(t/\tau + 1)e^{-t/\tau} - 1]$	$p \varepsilon \Phi t^2/2$	$p \varepsilon \Phi (1 - \varepsilon \lambda t) \tau t$
M_Z/M_\star	$\frac{p}{1-R} \left[1 - \varepsilon \lambda \tau \left(1 + \frac{((1+t/\tau)e^{-t/\tau} - 1)}{t/\tau + e^{-t/\tau} - 1} \right) \right]$	$\frac{p}{1-R}$	$\frac{p}{1-R} (1 - \varepsilon \lambda \tau)$

APPENDIX A: ANALYTICAL SOLUTION FOR CONSTANT INFLOW MODELS

In this section, we summarize the chemical evolution formalism of Peng & Maiolino (2014) and present further exact solutions for the metallicity and total metal content.

Peng & Maiolino (2014) models offer solutions for equations (1)–(4) under the following assumptions.

- (i) Constant inflow rate Φ .
- (ii) A linear relation star formation law $\text{SFR} = \varepsilon M_{\text{gas}}$, with constant ε .
- (iii) Outflow rate proportional to the SFR through a constant loading factor λ : $\Psi = \lambda \text{SFR}$.

We further assume that the net nucleosynthetic yield p and return factor R are constant with time and the inflow is of primordial gas (with zero metallicity). Under these assumptions, analytical solutions can be obtained with an explicit time dependence. As discussed in Peng & Maiolino (2014), the equilibrium timescale

$$\tau \equiv \frac{1}{\varepsilon (1 - R + \lambda)} \quad (\text{A1})$$

is the natural timescale driving the chemical evolution of the system. For $t \gg \tau$, physical properties of galaxies tend to their ‘equilibrium’ values. As discussed in Peng & Maiolino (2014), low-mass dwarf galaxies and chemically un-evolved systems will not satisfy the equilibrium condition and need to be studied in the $t < \tau$ regime.

In Table A1, we summarize the analytical solutions for a number of galaxy properties. We note that, apart from the assumptions stated above, the solutions are mathematically exact.⁵ We also remark that, as expected, the only timescale responsible for the chemical evolution of the system is the equilibrium timescale defined above (equation A1).

The limits of the solutions for the equilibrium case ($t \gg \tau$) have a simple physical interpretation. Star formation exactly balances out the inflow and outflow rates, the gas mass (and hence the SFR) stays constant and the stellar mass grows linearly with time. In this regime, the gas-phase metallicity plateaus at a constant value

$$Z_g(\text{eqm}) = p \varepsilon \tau = \frac{p}{1 - R + \lambda}, \quad (\text{A2})$$

which depends only on the net yield, the return fraction and the outflow loading factor. Note also that the equilibrium value of the M_Z/M_\star ratio is $\frac{p}{1-R}(1 - \varepsilon \lambda \tau)$, lower than the expected value

⁵ The solution to the gas-phase metallicity (Z_g) presented here differs from the one in Peng & Maiolino (2014), who solve for the metallicity evolution making further approximations to simplify the algebra.

$M_Z/M_\star = \frac{p}{1-R}$ in absence of outflows (i.e. for $\lambda = 0$). The gas fraction f_{gas} can be considered as a function of t , τ and ε , and is the best property to quantify the degree of chemical evolution of the system: systems with low gas fraction have not reached equilibrium and are chemically un-evolved, while systems with low gas fraction are in equilibrium and chemically evolved.

The analytical solutions are also an important tool to study the parameter dependences of different physical properties. In particular, we can easily show that the relation between M_Z/M_\star and f_{gas} depends only on the value of the outflow loading factor, and does not depend on the assumed inflow rate and star formation efficiency. In other words, the position of a point in the f_{gas} versus M_Z/M_\star plane depends only on λ . To prove this it is sufficient to observe that both f_{gas} and M_Z/M_\star are only a function of λ and t/τ . Therefore, eliminating t/τ , it would be possible to write a relation between f_{gas} and M_Z/M_\star which depends only on λ . Unfortunately, the complex nature of the solutions does not allow such relation to be written in closed form. Physically this statement can be interpreted as stating that the metal deficit (i.e. M_Z/M_\star) depends only on how evolved the system is (i.e. its f_{gas}) and the strength of its outflows (i.e. λ). As shown in Appendix B, this simple result is *not* valid anymore if we assume that the inflow rate is proportional to the SFR.

Finally, we note that exactly the same argument can be applied to the relation between f_{gas} and Z_g , which can therefore be shown to depend only on the outflow loading factor and not on the inflow rate and the star formation efficiency.

APPENDIX B: EQUILIBRIUM, TIMESCALES AND INFLOW RATES IN DIFFERENT ‘BATHTUB’ MODELS

In this section, we briefly recap the main features and differences between the growing set of chemical evolution ‘bathtub’ models. We will focus on a comparison of the models presented in Davé, Finlator & Oppenheimer (2011), Lilly et al. (2013), Dayal et al. (2013) and Peng & Maiolino (2014), the latter being our reference model. The casual reader is encouraged to read the summary at the end of this section.

A ‘bathtub’, or ‘gas regulatory’ model, is defined here to be a system assumed to obey the equations (1)–(4). An ‘ideal’ bathtub model is one in which we assume

- (i) a linear relation star formation law $\text{SFR} = \varepsilon M_{\text{gas}}$, with constant ε ;
- (ii) outflow rate proportional to the SFR through a constant loading factor λ : $\Psi = \lambda \text{SFR}$.

The simplest bathtub model, like the one presented in Davé et al. (2011), is an ‘equilibrium’ model. An equilibrium model is defined

by the assumption that the gas mass in the system does not change with time ($dM_{\text{gas}}/dt = 0$). This assumption is justified by Davé et al. (2011) on grounds of its relevance to cosmological hydrodynamical simulations. In equilibrium, equation (1) reduces to

$$\Phi = (1 - R + \lambda) \text{SFR} \quad (\text{eqm}). \quad (\text{B1})$$

Note that even in an equilibrium model the SFR will change in time; however, equilibrium requires that it does so at the same rate as the inflow rate. The same conclusion is evident in the equilibrium solution for the SFR presented in Table A1 above.

Davé et al. (2011) also argue that, when departures from equilibrium are allowed, the bathtub model naturally generates a secondary dependance of the mass–metallicity relation on SFR, in the sense that more gas-rich systems will have higher SFR and lower metallicities. This feature of the model is generally considered a success (Lilly et al. 2013), since it is capable of reproducing the observed fundamental metallicity relation (Mannucci et al. 2010; Andrews & Martini 2013). Moreover, this feature is mostly independent of the detailed time-evolution of the cosmological inflow rate, since it is just a general characteristic of the non-equilibrium bathtub models.

Subsequent work in Lilly et al. (2013) has shown that equilibrium is generally a good assumption for gas-poor, chemically evolved, massive low-redshift galaxies, while it is not a good assumption for the gas-rich dwarfs or galaxies at high redshift (see in particular sections 2.3 and 2.4 of Lilly et al. 2013 for a detailed discussion of the relevant timescales and section 5 of Peng & Maiolino 2014 for an estimate of the equilibrium timescale for gas-rich systems). It is therefore clear that in applying the bathtub model to the chemically un-evolved, gas-rich outer disc of NGC 628, a model that takes into account departure from equilibrium is needed.

The simplicity of the framework offered by the bathtub model has encouraged several authors to seek analytical solutions for its fundamental equations. Unfortunately, if we do not assume the system is in equilibrium, the relation between metallicity and gas fraction (which can be interpreted as natural ‘clock’ in the context of chemical evolution) will depend on the assumed time evolution of the inflow rate.

A notable special case is represented by the popular solutions for the case in which the inflow rate is proportional to the SFR (Matteucci & Chiosi 1983; Dayal et al. 2013; Kudritzki et al. 2015). The success of these solutions is to be attributed to the fact that they are arguably the simplest example of non-equilibrium models (i.e. $dM_{\text{gas}}/dt \neq 0$) which have closed-form analytical solutions. As all non-equilibrium bathtub models, they show the usual behaviour of tending to equilibrium at late times and predict a secondary relation on SFR in the mass–metallicity relation (Dayal et al. 2013). However, we warn the reader against fallaciously reversing the argument, i.e. the existence of the fundamental metallicity relation does not necessarily imply that the inflow rate must be proportional to the SFR.

It is important to stress that, while the other assumptions made in the context of the bathtub model can be justified, albeit approximately, on physical or observational grounds, there is no physical or observational reason to believe that the inflow rate should follow the same time evolution as the SFR when the system is not in equilibrium. Confusion often arises in the literature because, in equilibrium, all bathtub models predict the time evolution of the SFR to the follow that of the inflow rate. However, this conclusion is only true when the system is at equilibrium and *not* true in general as the system approaches equilibrium.

On the other hand, the cosmological inflow rate follows a well-defined trend with halo mass and redshift. Both semi-analytics and

cosmological simulations demonstrate that the halo accretion rate can be parametrized as

$$\frac{dM_h}{dt} = \alpha M_h (1+z)^\beta, \quad (\text{B2})$$

where M_h is the halo mass and $\alpha \sim 0.030 \text{ Gyr}^{-1}$ and $\beta \sim 2.5$ (Dekel et al. 2013). For an Einstein-de-Sitter universe, equation (B2) admits a particularly simple solution leading to

$$M_f = M_i e^{-a(z_f - z_i)}, \quad a = \alpha / (H_0 \Omega_m^{1/2}) \sim 0.8, \quad (\text{B3})$$

where the subscripts f and i refer to final/initial masses and redshifts. Therefore, by substituting back into equation (B2), the halo mass accretion rate at redshift z , $\dot{M}_h(z)$ is given by

$$\dot{M}_h(z) = 0.03 M_i e^{-a(z_f - z_i)} (1+z)^{2.5}. \quad (\text{B4})$$

As reported in previous work (Dekel et al. 2013; Lilly et al. 2013), this halo accretion rate does not evolve very much over most of the age of the Universe. In particular, it changes by about a factor of 2 between $z = 5$ and 0.3. We neglect here that fact that only a fraction of accreting baryons will reach the galaxy disc and are thus available for star formation, and this fraction might be a complex function of mass, redshift and perhaps other quantities (environment). Under these assumptions, Peng & Maiolino (2014) argue that the inflow timescale is much longer than all other timescales relevant to galaxy evolution (including the equilibrium timescale) and, therefore, it is an excellent approximation to assume the gas-inflow rate to be constant in time. By making the assumption that the timescale for changes in the infall rate is much longer than the equilibrium timescale, we obtain the models presented in Table A1, which have been used throughout this paper.

To demonstrate the physical difference between the solutions that assume a constant inflow rate and the solutions which assume the inflow rate to be proportional to the SFR at all times, we present a comparison of their time evolution. The first thing to appreciate is that, if we assume the inflow rate proportional to the SFR ($\Phi = \omega \text{SFR}$), equation (1) only admits the following solution for the gas mass M_g

$$\frac{dM_g}{dt} = (\omega - \lambda - 1 + R)\varepsilon M_g \rightarrow M_g = M_0 e^{-(1-R-\omega+\lambda)\varepsilon t}, \quad (\text{B5})$$

where M_0 is the initial gas reservoir at $t = 0$. Physical solutions require $1 - R - \omega + \lambda > 0$, and hence imply an exponentially declining SFR. The gas equilibrium timescale (τ') for this model depends on ω and is given by

$$\tau' = \frac{1}{\varepsilon(1 - R + \lambda - \omega)}. \quad (\text{B6})$$

This timescale tends to the timescale in A1 for small ω . We therefore refer to the model with SFR proportional to the inflow rate as an ω -model. The equilibrium behaviour of the ω -model is very different from the constant inflow regulator. In the ω -model, equilibrium can only be reached for $\text{SFR} = \varepsilon M_g = 0$. Because of its defining assumption, this model implicitly assumes the inflow rate ($\Phi = \omega \text{SFR}$) to be exponentially declining (unless we wish to build a more general model with a different star formation law, i.e. $\text{SFR} \neq \varepsilon M_g$, which we will not discuss here). In light of the discussion on the cosmological accretion rate above, this is a much worse parametrization than the assumption of a constant inflow rate. However, an exponentially declining inflow rate is still a useful model in the context of the overall evolution of galaxies, since it can represent the shutdown of star formation due to a declining inflow rate. This model is therefore similar to the ‘strangulation’ models

Table B1. Exact analytical time-dependent solution of the ideal regulator with inflow rate proportional to the SFR ($\Phi = \omega$ SFR) for different galaxy properties. Note that M_0 below refers to the gas mass at $t = 0$ and τ' is the gas equilibrium timescale defined in equation (B6).

Galaxy property	Exact solution	$t = 0$	$t \gg \tau'$
M_g	$M_0 e^{-t/\tau'}$	M_0	0
$\text{SFR} = \varepsilon M_g$	$\varepsilon M_0 e^{-t/\tau'}$	εM_0	0
M_\star	$M_0 \tau' \varepsilon (1 - R) (1 - e^{-t/\tau'})$	0	$M_0 \tau' \varepsilon (1 - R)$
$f_{\text{gas}} \equiv \frac{M_g}{M_g + M_\star}$	$\left[1 + \varepsilon \tau' (1 - R) (e^{t/\tau'} - 1)\right]^{-1}$	∞	0
$Z_g \equiv M_{Zg}/M_g$	$\frac{p}{\omega} (1 - e^{-\omega \varepsilon t})$	0	$\frac{\varepsilon p}{\omega}$

used in Peng, Maiolino & Cochrane (2015) to study the buildup of the red sequence.

Although the relation between metallicity and gas mass in the ω -model has been widely used in the literature, it is instructive to present here the solutions for the time evolution of this model, which can be found in Table B1. We note that, unlike in the constant inflow model, the metallicity in the ω -model does not come to equilibrium on the gas equilibrium timescale defined in B6 but on the dilution timescale $\tau_{\text{dil}} \equiv (\varepsilon \omega)^{-1} = M_g/\Phi$. Therefore, the final relation between metallicity and gas content will depend on combination of the gas equilibrium and the dilution timescales. In particular, by combining the solutions for Z_g and M_g , we obtain the well-known relation

$$Z_g = \frac{p}{\omega} \left(1 - \left(\frac{M_g}{M_0} \right)^{\omega/(1-R-\omega+\lambda)} \right), \quad (\text{B7})$$

and by combing the solution for M_\star and M_g , we can eliminate M_0 from the above and re-write the metallicity in the ω -model completely in term of observables,

$$Z_g = \frac{p}{\omega} \left(1 - \left(\frac{M_\star}{M_g} (1 + w) \right)^{-\omega/(1-R-\omega+\lambda)} \right), \quad (\text{B8})$$

where $w \equiv (\lambda - \omega)/(1 - R)$. As can be explicitly seen from this equation, the relation between Z_g and gas fraction depends on the inflow rate (through ω), causing the observed degeneracy in the determination of ω and λ when using this model.

Following is the summary.

(i) Equilibrium (defined by the requirement $dM_{\text{gas}}/dt = 0$) bathtub models predict the SFR to be proportional to the inflow rate.

(ii) Non-equilibrium bathtub models tend to equilibrium at late times. These models can naturally reproduce the fundamental metallicity relation (i.e. imply an SFR dependance in the mass–metallicity relation).

(iii) The cosmological accretion rate, as calculated using semi-analytics or cosmological simulations, is slowly varying over most of the age of the Universe. Hence, a constant gas-inflow rate is generally a good assumption for the purpose of chemical evolution modelling. In a constant inflow model, the relation between metallicity and gas fraction depends only on the outflow loading factor and not on the inflow rate.

(iv) Non-equilibrium models which fix the inflow rate to be proportional to the SFR implicitly assume the inflow rate to be exponentially declining. This is not a good representation of the cosmological accretion rate for ‘main-sequence’ star-forming galaxies, but could constitute a good model for strangulation, as in Peng et al. (2015). Moreover, in this model the relation between the metallicity and the gas fraction depends on both the outflow loading factor and the proportionality factor between inflow rate and SFR, causing a degeneracy between inflows and outflows when interpreting metallicity data.

This paper has been typeset from a $\text{\TeX}/\text{\LaTeX}$ file prepared by the author.